Numerical Study of Reaction-Diffusion Systems using Front Tracking

A Dissertation presented

by

Saurabh Gajanan Joglekar

to

The Graduate School

in Partial Fulfillment of the

Requirements

for the Degree of

Doctor of Philosophy

in

Applied Mathematics and Statistics

(Concentration - Computational Applied Mathematics)

Stony Brook University

August 2017

Stony Brook University

The Graduate School

Saurabh Gajanan Joglekar

We, the dissertation committe for the above candidate for the

Doctor of Philosophy degree, hereby recommend

acceptance of this dissertation

Xiaolin Li - Dissertation Advisor
Professor, Department of Applied Mathematics and Statistics

Roman Samulyak - Chairperson of the Committee
Professor, Department of Applied Mathematics and Statistics

Hyunkyung Lim
Research Assistant Professor,
Department of Applied Mathematics and Statistics

Yangang Liu
Senior Scientist, Brookhaven National Laboratory,
Environmental and Climate Sciences Department

This dissertation is accepted by the Graduate School

Charles Taber
Dean of the Graduate School

Abstract of the Dissertation

Numerical Study of Reaction-Diffusion Systems using Front Tracking

by

Saurabh Gajanan Joglekar

Doctor of Philosophy

in

Applied Mathematics and Statistics

(Concentration - Computational Applied Mathematics)

Stony Brook University

2017

We study the three component Reaction-Diffusion systems with and without precipitation and crystal growth. Focus is on the generic chemical reaction represented by $nA + mB \longrightarrow C$, where n, m are the stoichiometric coefficients. In case of the reaction-diffusion system without precipitation, we investigate the movement of the center of reaction zone in for equal and unequal diffusivities. We compare the analytical and numerical solutions for equal diffusivities to establish the accuracy of the numerical method. Then we apply the numerical method to provide numerical evidence in support of a conjecture in the case of unequal diffusivities.

Next, we apply the Front Tracking method to study the reaction-diffusion systems with crystal growth in higher spatial dimentions. The effects of different parameters on the crystal growth are investigated.

Key words: Reaction-Diffusion System, Reaction-Diffusion Equations, Reaction zone/front, Center of reaction front, front tracking, crystal growth.

To my father, my mother and my wife.

Contents

List of Figures

List of Tables

List of Abbreviations

Abbreviation	**Meaning**
BC	Boundary Condition/s
DLA	Diffusion Limited Aggregation
IC	Initial Condition/s
ODE	Ordinary Differential Equation/s
PDE	Partial Differential Equation/s
RDE	Reaction-Diffusion Equation/s
RDP	Reaction-Diffusion Process
RDS	Reaction-Diffusion System

Acknowledgements

This dissertation would not have been possible without the help of many people in many ways. I owe my gratitude to all those people who made this journey possible and who made the experience memorable.

I would like to express my sincere gratitude to my advisor, Prof. Xiaolin Li for his valuable advice, support and guidance. He taught me the skills and expertise required to finish my PhD study and many other nuances in the broad field of scientific computing. The fluency with which he applies his computational skills to various scientific problems has always been a source of inspiration for me.

I am also indebted to Prof. Xiangmin Jiao and Prof. Jin Wang who shared valuable scientific insights regarding my dissertation topic. I am also thankful to Prof. Roman Samulyak who served as my course instructor during the begining of my studies. He was essentially the first person who introduced me to the mathematical knowledge required for scientific computing and I learned a lot from him. He also provided important insights into my dissertation. I would also like to thank Prof. Hyunkyung Lim and Dr. Yangang Liu for being on my dissertation committee. I would like to acknowledge the support of the Department of Applied Mathematics and Statistics and it's staff. This work was supported in part by the equipment grant by the US Army Research Office under the ARO-DURIP Grant W911NF1210357.

I would like to thank all my friends in my research group for their friendship and encouragement. I wish to mention JoungDong Kim, Yan Li, Yijing Hu, Yiyang Yang, Qiangqiang Shi, Zheng Gao, Xiaolei Chen, Muye Chen and Tengbo Yang.

I would also like to mention my friends Omkar Aphale, Akshay Patil, Ravi Dey, Niranjan Hasabnis, Sujan Dabholkar and Pralhad Deshpande who made this journey enjoyable.

Most importantly, I wish to thank my mother Dr. Seema Joglekar, my father Dr. Dilip Joglekar and my wife Charuta. Their support and unconditional love gives me strength at every step of the way in my life. This dissertation is dedicated to them.

Chapter 1

Introduction

Study of crystal formation and growth in a solution is an active research area in physical chemistry. Crystallization is a process used to obtain a near pure substance in solid form. There are various mechanisms responsible for crystal growth. A comprehensive list of these mechanisms is provided in [11]. In the current work, front tracking method has been applied to one of these mechanisms, *precipitation by the (isothermal) addition of reactive components or solvent components to reduce solubility (addition by diffusion or with stirring)* [11]. This mechanism also applies to multi-component systems. In the absence of convection, such systems are characterized by reaction and diffusion. In a single component Reaction-Diffusion system, reaction is primararily the precipitation reaction. In multicomponent systems, different substances in solution form react with each other to produce a substance, which deposits under suitable physical conditions to form a solid precipitate.

The mechanism of crystallization mentioned above is explained through Diffusion Limited Aggregation (DLA) [14]. On microscopic level, dissolved solute particles perform Brownian motion in the solvent. On contact, the particles adhere to each other irreversibly. When the congregated mass is large enough, it forms the precipitate. Thus, if a seed particle is fixed at the center of some coordinate system and solute particles are allowed to perform random walk, the particles will eventually attach themselves irreversibly to the seed and the cluster will grow. This model produces highly branched and fractal structure as shown in [14]. Fractal structure is due to the fact that faster growing parts of the cluster shield other parts, thus making them less accessible to free particles which are still performing ramdom walk. Although the model is simple, the problem becomes computationally intractable as the number of particles grows larger.

On the macroscopic scale, the growth of dendrites is described by a system of partial differential equations.Mathematically, these processes are governed by a system of Reaction-Diffusion Equations (henceforth abbreviated RDE's). Typically, RDE's are parabolic PDE's coupled through the source term. They represent a moving boundary problem. Considerable amount of theoretical and experimental work has been done on single as well as multi-component Reaction-Diffusion systems. Analytical (closed-form) solutions are available only for the simplest of the cases and boundary conditions. For the non-homogeneous cases in which the precipitation front evolves with time, numerical simulations and laboratory experiments are the main tools of investigation. Behaviour of a given Reaction-Diffusion system and the patterns formed within the system can vary greatly depending upon nature of reaction term. We focus mainly on the dendritic growth and Liesegang pattern formation.

Following section gives a review of the experimental and numerical work done and reported by so far. This short review concerns the Reaction-Diffusion systems with and without the precipitation involved. Emphasis has been given on the mathematical description of the problems.

1.1 Crystal Formation and Dendritic Growth

Xiaolin Li et al [1] have studied a single component Reaction-Diffusion system through front tracking without consideration of advection, in which the reaction term is replaced by precipitation term at the fluid-solid interface. The governing equations for the solute concentration $C = C(\vec{x}, t)$ are as follows:

$$\frac{\partial C}{\partial t} = D\nabla^2 C, \quad for\ \vec{x} \in \Omega \tag{1.1}$$

Here Ω is the ambient region containing solute and D is diffusion coefficient. At the fluid-solid interface $\partial\Omega$, the front growth is governed by:

$$D\frac{dC}{dn}(\vec{x_s}) = k\big(C(\vec{x_s}) - C_e\big) \tag{1.2}$$

where k is the reaction rate per unit area for the solute from the liquid phase to precipitate onto the solid phase at the interface, C_e is the equilibrium concentration and $C(\vec{x_s})$ is the local concentration of solute at the interface. Interface is propagated with the normal velocity,

$$\upsilon_n = \frac{D}{\rho_s}\frac{dC}{dn}(\vec{x_s}) \tag{1.3}$$

where ρ_s is the density of solid phase. Interface growth and the dendritic structure of the precipitate have been studied at different Damkohler numbers. Front tracking is well suited to dendritic structures at large Damkohler numbers where high resolution is necessary.

Tartakovsky et al [3] have studied multi-component Reaction-Diffusion systems for the chemical reaction $A+B \longrightarrow C_{(aq+solid)}$, on two different spatial scales, Pore-scale and Darcy-scale. Smoothed particle hydrodynamics (SPH) has been applied to carry out hybrid simulations on two different spatial scales. Let $A(\vec{x},t),\ B(\vec{x},t),\ C(\vec{x},t)$ and $D_a,\ D_b,\ D_c$ be the concentrations and diffusion coefficients of components $A,\ B$ and C in solute phase. Let k and k_{AB} be heterogeneous and homogeneous reaction rates and ρ_s be the density of solid phase. Then the Pore scale model satisfies following system of equations:

$$\begin{aligned}
\frac{\partial A}{\partial t} &= \nabla \cdot (D_a \nabla A) - k_{AB}AB && (1.4)\\
\frac{\partial B}{\partial t} &= \nabla \cdot (D_b \nabla B) - k_{AB}AB && (1.5)\\
\frac{\partial C}{\partial t} &= \nabla \cdot (D_c \nabla C) + k_{AB}AB - k\int_{\mathbf{F}} H(C - C_{eq})\delta(\vec{x} - \vec{x}_f)\, d\vec{x}_f && (1.6)
\end{aligned}$$

where $H(x)$ is the Heaviside step function and the integration is taken over the whole fluid-solid interface. Soluble precipitate C follows the first order kinetic reaction model on the fluid-solid interface,

$$D_c\frac{dC}{dn} = k\big(C - C_{eq}\big) \tag{1.7}$$

The interface advances into the liquid with normal velocity,

$$\upsilon_n(\vec{x}_s) = \frac{A_0 + B_0}{\rho_s} D_c \nabla C \cdot \vec{n} \tag{1.8}$$

Simulations start with a crystal seed already present in the domain. Hence, although the same equations govern the formation of Liesegang Patterns, nucleation theories have not been considered in Tartakovsky et al [3].

1.2 Liesegang Pattern Formation

Another type of precipitation pattern commonly observed in chemical systems is the Liesegang pattern. When an outer electrolyte A is put on top of an inner electrolyte B and the diffusion is allowed to take place through a chemically inert medium like gel, peculiarly spaced precipitation patterns are observed throughout the medium, typically when advection is absent. Usually the precipitation patterns consist of bands, rings or spherical shells. Shape of the pattern depends on the geometry of the experimental setup. Extensive theoretical and numerical studies have been done since the discovery of the phenomenon almost a century ago. Supersaturation Theory, Sol-Coagulation and Phase Separation are three main models proposed to explain the formation of Liesegang patterns [4]. None of the theories have been fully successful in explaining macroscopic as well as microscopic structure of the Liesegang bands. Following figure shows Liesegang bands and rings obtained in a laboratory setup.

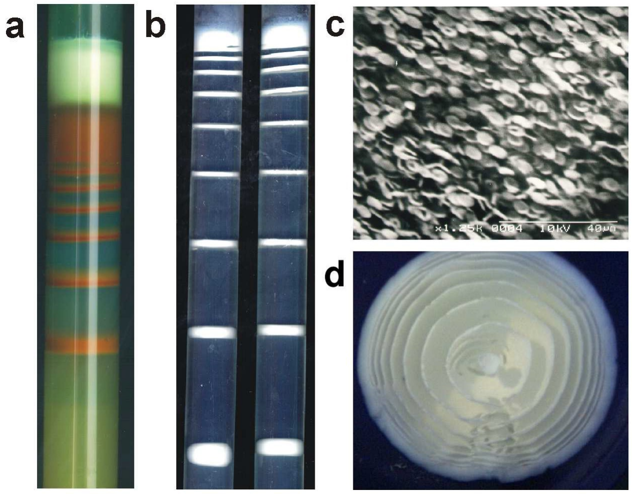

Figure 1.1: Liesegang banding of (a) $CuCl_2 + K_2CrO_4$ system in silica gel column, and (b) that of $NH_4OH + MgCl_2$ system in PVA gel column. (c)Picture taken with Environmental Scanning Electron Microscopy of the colloidal particles that build up a Liesegang band formed in the experiment on panel (b). (d)Cross-section of Liesegang shells of $NH_4OH + MgCl_2$ system in PVA gel. (Source [10])

1.2.1 Supersaturation Theory

This is the simplest theory put forth by Wilhem Ostwald to explain Leisegang banding. In the simple form, it concerns the chemical reaction $A + B \xrightarrow{Chemical\ Reaction} C \xrightarrow{Precipitation} D$. Chemical species A ad B react to form C. The reaction front is assumed to propagate only through diffusion. As the reaction proceeds in time, the concentration of C keeps increasing in the wake of reaction front. Eventually it reaches saturation level. However, the precipitation does not start untill the local concentration at any point in te domain reaches a supersaturation point, called the nucleation threshold. Once the nucleation threshold is reached, species C forms localised colloidal particles, D. Typically, the threshold concentration required for growth of the particles is much less than the nucleation threshold. Hence, the precipitate grows rapidly starting at the point of nucleation. Eventually, the areas near the precipitate are depleted of C and the concentration drops below the precipitation threshold. As the reaction front moves forward through the domain, same process is repeated at specific points in the domain, thus giving rise to Liesegang bands. This process assumes that the species C does not undergo any diffusion and the nucleation is spontaneous.

This model was formulated mathematically by C. Wagner [15]. The model is able to reproduce the Liesegang bands and rings observed in laboratory setting. It was further improved by T. Antal and Z. Racz.[8]. At the next level of complexity is the case where species C diffuses through the medium in addition to forming the precipitate D. This has been explored in [8].

In most of the numerical simulations, supersaturation theory is the primary model of nucleation. For the sake of completeness, Sol Coagulation theory and Phase Separation theory have been explained below in brief.

1.2.2 Sol Coagulation Theory

Experiments performed in [17] and [18] suggest that Supersaturation theory cannot explain all the experimental findings in a laboratory setting. They also suggest that formation of the bands is a process occuring after the reaction, and not primarily related to it. Sol coagulation models [8] and [16] propose that the band formation takes place in two different stages. The first stage consists of formation of colloidal sol after the concentration of C reaches nucleation threshold.

This sol is not observable by the naked eye. The precipitation bands are later formed from the coagulation of sol, after the ionic concentration reaches *critical coagulation concentration.*

Both Supersaturation theory and Sol Coagulation theory predict that the precipitation bands are formed one at a time. However, the experimental findings reported by H. Higuchi and R. Matura [19] suggest that this prediction is not always true. It has been suggested that the mechanism of the formation of Liesegang bands is specific to the chemical system under consideration. No universal theory has yet been proposed which explains all laboratory observations. Advantage of these theories is that they are easy to implement in numerical simulations. The disadvantage is the absence of parameter(s) which control the time at which the bands are formed, the spacing between bands and the width of bands.

1.2.3 Phase Separation Theory

Theories put forth in [20], [21], [22] propose that the reaction of A and B forms an intermediate product M which is capable of undergoing phase separation. Some time after the reaction front has swept past the region containing M, the intermediate product gets separated into high density regions and low density regions. High density regions appear as bands of the precipitate while low density regions cannot be observed by the naked eye. The process of the formation of M is governed by the following equation [10].

$$\frac{\partial m(x,t)}{\partial t} = -\lambda \frac{\partial^2}{\partial x^2}[\epsilon(m(x,t)-m_*)-\gamma(m(x,t)-m_*)^3+\sigma\frac{\partial^2}{\partial x^2}(m(x,t)-m_*)]+S(x,t) \tag{1.9}$$

The source term S represents the production rate of compound M by chemical reaction [10]. The advantage of this model over previous ones is the presence of parameters which can control the formation of bands.

1.2.4 Cellular Automata Model

B. Chopard, P. Luthi and M. Droz [4] have carried out numerical simulations based on cellular automata approach and supersaturation theory proposed by W. Ostwald [5]. Their model is concerned with the chemical reaction $A + B \xrightarrow{\textit{Chemical Reaction}} C \xrightarrow{\textit{Precipitation}} D$. Two chemical species A and B react to produce a species C which also diffuses. When local concentration of C reaches some threshold value, nucleation occurs spontaneously. Spontaneity of nucleation after supersaturation level is the basis for Supersaturation model of precipitation. Mathematical model is based on G. T. Dee [6]:

$$\partial_t a = \partial_x^2 a - \kappa ab \tag{1.10}$$

$$\partial_t b = \frac{D_b}{D_a}\partial_x^2 b - \kappa ab \tag{1.11}$$

$$\partial_t c = \frac{D_c}{D_a}\partial_x^2 c + \kappa ab - u \tag{1.12}$$

where D_i is the diffusion constant for species i, κ is the reaction constant and u is the nucleation and aggregation term. Different expressions for u in Dee [6] and Le Van and Ross [7] lead to different systems of coupled nonlinear PDE's which, when solved numerically, lead to Liesegang bands.

Horvat and Hantz [23] have also carried out the simulations using the cellular automata approach and supersaturation thoery. The governing equations are:

$$\frac{\partial a(x,y,t)}{\partial t} = D_a(x,y)\cdot\nabla^2 a(x,y,t) - r\cdot a(x,y,t)\cdot b(x,y,t) \tag{1.13}$$

$$\frac{\partial b(x,y,t)}{\partial t} = D_b(x,y)\cdot\nabla^2 b(x,y,t) - r\cdot a(x,y,t)\cdot b(x,y,t) \tag{1.14}$$

$$\frac{\partial c(x,y,t)}{\partial t} = D_c(x,y)\cdot\nabla^2 c(x,y,t) + r\cdot a(x,y,t)\cdot b(x,y,t) - [R] \tag{1.15}$$

The cellular automata rules are given by:

$$\begin{array}{lll}
(R0): & [c(x,y,t) > c^{**}] \wedge [d(x,y,t) = \text{empty}] & \longrightarrow \quad d(x,y,t+\Delta t) = \text{active} \\
(R1): & [c(x,y,t) > c^{*}] \wedge [d(x,y,t) = \text{active}] & \longrightarrow \quad [d(x_{nn},y_{nn},t+\Delta t) \\
& & \qquad = \text{active}] \\
& & \quad \wedge [d(x,y,t+\Delta t) \\
& & \qquad = \text{bulk precipitate}] \\
& & \quad \wedge [c(x,y,t+\Delta t) = 0] \\
(R2): & [c(x,y,t) < c^{*}] \wedge [d(x,y,t) = \text{active}] & \\
& \qquad \wedge [T(x,y,t) \leq \tau(\upsilon)] & \longrightarrow \quad T(x,y,t+\Delta t) \\
& & \qquad = T(x,y,t) + \Delta t \\
(R3): & [c(x,y,t) < c^{*}] \wedge [d(x,y,t) = \text{active}] & \\
& \qquad \wedge [T(x,y,t) > \tau(\upsilon)] & \longrightarrow \quad d(x,y,t+\Delta t) = \text{passive} \\
(R4): & [d(x,y,t) = \text{active}] & \\
& \wedge [d(x_{nn},y_{nn},t) = \text{nonempty} \; \forall \; (x_{nn},y_{nn})] & \longrightarrow \quad d(x,y,t+\Delta t) \\
& & \qquad = \text{bulk precipitate}
\end{array}$$

$$\begin{aligned}
D_a(x,y) = &\quad 0, \qquad \text{if } d(x,y) = \text{passive or obstacle} \\
= &\quad D_a, \qquad \text{otherwise}
\end{aligned}$$

$$\begin{aligned}
D_{b,c}(x,y) = &\quad 0, \qquad \text{if } d(x,y) = \text{nonempty} \\
= &\quad D_{b,c}, \qquad \text{otherwise}
\end{aligned}$$

Here $a(x,y,t)$ and $b(x,y,t)$ represent the ion concentrations of species A and B respectively. $c(x,y,t)$ is the concentration of diffusive intermediate product C. $d(x,y,t)$ identifies whether precipitate is present in the cell or not. It is not related to concentrations. c^{**} is the nucleation threshold and c^{*} is growth threshold. $[R]$ signifies the cellular automata rules dictated by supersaturation theory. $\wedge$ is the logical AND operator. $T(x,y,t)$ is the age and $\tau(\upsilon)$ is the maximal lifetime of the cells. υ is the speed of propagation of the precipitation front. The maximal lifetime is assumed to be a function of υ. (x_{nn}, y_{nn} are the nearest neighbors of the lattice point (x,y).

1.2.5 Spacing and Width Laws

The position, width and the time at which various Liesegang bands are formed seem to follow certain empirical laws. Numerical verification of these laws can be found in [4]. Let x_n be the position of the n-th Liesegang band, w_n be it's width and t_n be the time at which nucleation was first observed in n-th band. The law $x_n \sim \sqrt{t_n}$ is well satisfied[4] and is the signature of diffusion process. The width law $w_n \sim x_n^{\alpha}$ is also shown to be satisfied numerically[4].

T. Antal et al [8] have done theoretical and numerical investigations into the Matalon Packter Law[9] for the precipitation reaction stated above. Mathematical model they have used is as follows:

$$\frac{\partial a}{\partial t} = D_a \frac{\partial^2 a}{\partial x^2} - k\theta(ab - q^*) - \lambda abd \tag{1.16}$$

$$\frac{\partial b}{\partial t} = D_b \frac{\partial^2 b}{\partial x^2} - k\theta(ab - q^*) - \lambda abd \tag{1.17}$$

$$\frac{\partial d}{\partial t} = k\theta(ab - q^*) + \lambda abd \tag{1.18}$$

where D_a and D_b are diffusion coefficients, $\theta(x)$ is the step function, q^* is the nucleation threshold, k is the rate constant and λ is the aggregation constant. If a_0, b_0 represent the initial concentrations, then the initial conditions to the above equations are given by $a(x, 0) = a_0\theta(-x)$, $b(x, 0) = b_0\theta(-x)$, $d(x, 0) = 0$.

Chapter 2

Effectively One-dimensional Reaction-Diffusion Systems

In this chapter, we focus our attention on RDE's containing only one spatial dimension. The precipitation term will be absent for our current numerical investigations. The purpose of this chapter is to investigate the effect of different parameters on the solutions.

Consider a long thin tube which is open at both ends. At each end, there is a reactant present whose concentrations are maintained to be constants by external means. The tube is filled with an inert medium like a gel which does not take part in the chemical reaction. Let's assume that the reactants are denoted by A and B and their product is C. This experimental setup is similar to that for the formation of Liesegang patterns described in the previous chapter. The important difference is that the reactants may not necessarily be in direct contact with each other. Let us denote the diffusivities of A, B and C by D_a, D_b and D_c respectively. Let us also denote the homogeneous reaction constant by k_{AB}. Let us also denote the concentrations of A, B and C by A, B and C. This should not cause any ambiguity since the meaning will usually be clear from the context in which these symbols are used. Assume further that the tube has its left end located at $x = L$ and the right end at $x = U$. Then, for the chemical reaction $A_{(aq)} + B_{(aq)} \longrightarrow C_{(aq)}$, the evolution of the concentrations A, B and C is governed by the following system of RDEs:

$$\frac{\partial A}{\partial t} = D_a \nabla^2 A - k_{AB} A B \qquad (2.1)$$

$$\frac{\partial B}{\partial t} = D_b \nabla^2 B - k_{AB} A B \qquad (2.2)$$

$$\frac{\partial C}{\partial t} = D_c \nabla^2 C + k_{AB} AB \tag{2.3}$$

Although the diffusion term contains the partial derivatives in all spatial dimensions (i.e. the terms $\nabla^2 A$, $\nabla^2 B$ and $\nabla^2 C$), the experimental setup (long thin tube) allows us to focus on just one spatial dimension (along the length of the tube) and neglect the rest of the spatial dimensions. Hence ∇^2 can be replaced by $\frac{\partial^2}{\partial x^2}$. Thus the effectively 1D system of RDEs can be written as:

$$\frac{\partial A}{\partial t} = D_a \frac{\partial^2 A}{\partial x^2} - k_{AB} AB \tag{2.4}$$

$$\frac{\partial B}{\partial t} = D_b \frac{\partial^2 B}{\partial x^2} - k_{AB} AB \tag{2.5}$$

$$\frac{\partial C}{\partial t} = D_c \frac{\partial^2 C}{\partial x^2} + k_{AB} AB \tag{2.6}$$

The domain is $(x,t) \in \Omega = [L,U] \times [0,\infty)$. Boundary conditions (BCs) imposed are similar to [3]. i.e. $A(L,t) = 1,\ A(U,t) = 0,\ B(L,t) = 0,\ B(U,t) = 1,\ C(L,t) = C(U,t) = 0$. Initial conditions (ICs) $A(x,0) = f(x),\ B(x,0) = g(x),\ C(x,0) = h(x)$ will be specified later in numerical results.

2.1 Steady State Solutions

The purpose of the this section is to discuss the steady state solutions to RDEs (2.4) to (2.6). First we derive an ODE which governs the steady state solution. In the numerical results section, we investigate the effect of parameters on the solution.

2.1.1 Mathematical Analysis of the Steady State

We discuss the steady state solution to the system (2.4) to (2.6). In the steady state, $\lim\limits_{t\to\infty} \frac{\partial A}{\partial t} = \lim\limits_{t\to\infty} \frac{\partial B}{\partial t} = \lim\limits_{t\to\infty} \frac{\partial C}{\partial t} = 0$. Hence the system (2.4) to (2.6) is reduced to:

$$\begin{aligned} D_a\frac{d^2A}{dx^2} &= k_{AB}AB && (2.7)\\ D_b\frac{d^2B}{dx^2} &= k_{AB}AB && (2.8)\\ D_c\frac{d^2C}{dx^2} &= -k_{AB}AB && (2.9)\end{aligned}$$

where $x \in [L,U]$ and the boundary conditions are given by $A(L)=1,\ A(U)=0,\ B(L)=0,\ B(U)=1,\ C(L)=C(U)=0$. It can be deduced by simple calculations that

$$\begin{aligned} \frac{d^2(D_aA-D_bB)}{dx^2} &= 0 && (2.10)\\ \frac{d^2(D_aA+D_cC)}{dx^2} &= 0 && (2.11)\end{aligned}$$

This system of ODE's gives

$$\begin{aligned} B &= \frac{D_a}{D_b}A - m_{_B}x - c_{_B} && (2.12)\\ C &= \frac{D_a}{D_c}A + m_{_C}x + c_{_C} && (2.13)\end{aligned}$$

where the constants $m_{_B}$, $c_{_B}$, $m_{_C}$ and $c_{_C}$ are determined by the boundary conditions and are given by,

$$\begin{aligned} m_{_B} &= -\frac{1+\frac{D_a}{D_b}}{U-L} && (2.14)\\ c_{_B} &= \frac{L+U\,\frac{D_a}{D_b}}{U-L} && (2.15)\\ m_{_C} &= -\frac{1}{U-L}\,\frac{D_a}{D_c} && (2.16)\\ c_{_C} &= \frac{U}{U-L}\,\frac{D_a}{D_c} && (2.17)\end{aligned}$$

From equation (2.7) and (2.12), the steady state concentration of A is given by the ODE,

$$\frac{d^2A}{dx^2} = \frac{k_{AB}}{D_a}\,\frac{D_a}{D_b}\,A^2 - m_{_B}\,\frac{k_{AB}}{D_a}\,xA - c_{_B}\,\frac{k_{AB}}{D_a}\,A \qquad (2.18)$$

with boundary conditions $A(L) = 1,\ A(U) = 0$. Similar ODEs can be derived for B and C. Alternatively, expressions for B and C can be found by substituting A in (2.12) and (2.13) respectively. Unfortunately, equation (2.18) cannot be solved analytically in closed form. Thus, none of A, B and C can be expressed in closed form mathematical expressions. However, it is clear that the steady state solutions are governed by k_{AB}, $\frac{D_a}{D_b}$ and $\frac{D_a}{D_c}$. The effect of these parameters on the solution as well as the rate at which the system attains steady state is discussed in the section on numerical results.

2.1.2 Numerical Results for the Steady State Solution

In this section we present the steady state solution to the system (2.4) to (2.5) with the stated boundary conditions. Crank Nicolson method was used to discretize the PDE's. In each of the numerical tests, the program execution was terminated when the L_2-norm of the residual of solution vectors at two successive time steps was less than $\varepsilon = 10^{-15}$. The initial condition for C was uniformly set to $C(x,0) = h(x) = 0$ for all $x \in \Omega = [L, U]$. For the initial condition $A(x,0) = f(x)$, following functions were used in different numerical tests. They are simple test functions. All of them are continuous and piecewise smooth. The smooth pieces consist of linear, cosine and polynomial functions.

$$
\begin{array}{rcll}
 & & 1, & x \leq L, \\
f_1(x) & = & 0.5 + 0.5\cos\left(5\pi \dfrac{x-L}{U-L}\right), & L < x < \dfrac{4L+U}{5} \\
 & & 0, & x \geq \dfrac{4L+U}{5}
\end{array}
\qquad (2.19)
$$

$$
\begin{array}{rcll}
 & & 1, & x \leq L, \\
f_2(x) & = & \dfrac{U-x}{U-L}, & L < x < U \\
 & & 0, & x \geq U
\end{array}
\qquad (2.20)
$$

$$f_3(x) = \begin{array}{ll} 1, & x \leq L, \\ \frac{27}{4(U-L)^3}\left(x - \frac{4L-U}{3}\right)\left(x - \frac{L+2U}{3}\right)^2, & L < x < \frac{L+2U}{3} \\ 0, & x \geq \frac{L+2U}{3} \end{array} \tag{2.21}$$

$$f_4(x) = \begin{array}{ll} 1, & x \leq L, \\ \frac{9}{4(U-L)^2}\left(x - \frac{L-2U}{3}\right)\left(x - \frac{L+2U}{3}\right), & L < x < \frac{L+2U}{3} \\ 0, & x \geq \frac{L+2U}{3} \end{array} \tag{2.22}$$

$$f_5(x) = \begin{array}{ll} 1, & x \leq L, \\ 1 - \frac{5(U-x)}{2(U-L)}, & L < x < \frac{3L+2U}{5} \\ 0, & x \geq \frac{3L+2U}{5} \end{array} \tag{2.23}$$

The initial conditions $B(x,0) = g(x)$ for $x \in [L,U]$ are obtained by reflecting $f_j(x)$ about $x = \frac{L+U}{2}$, i.e. $g_j(x) = f_j(L+U-x)$, $j = 1,2,3,4,5$. In all of the the following tests, we have used $L = 0$ and $U = 1$. Figure 2.1 shows the initial concentration profiles of A, B and C. Figure 2.2 shows the effect of changing D_b on the steady state solution, with initial conditions as prescibed in Figure 2.1, and keeping other parameters constant. In all of the following figures, the blue curve represents A, the green curve represents B and the red curve represents C.

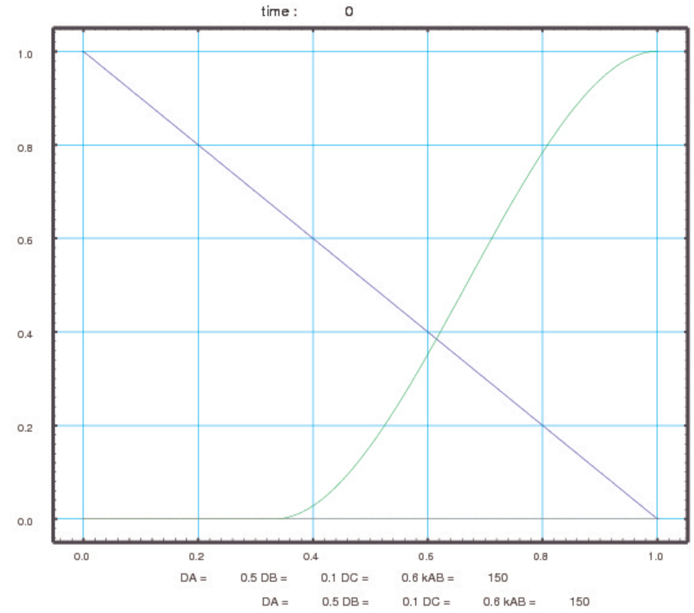

Figure 2.1: Concentration profiles at $t = 0$. $A(x,0) = f_2(x)$, $B(x,0) = g_3(x)$, $C(x,0) = 0$.

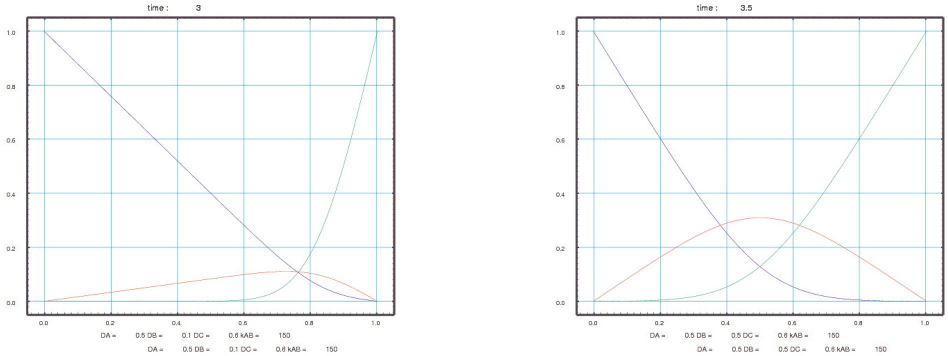

(a) $D_b = 0.1$ (b) $D_b = 0.5$

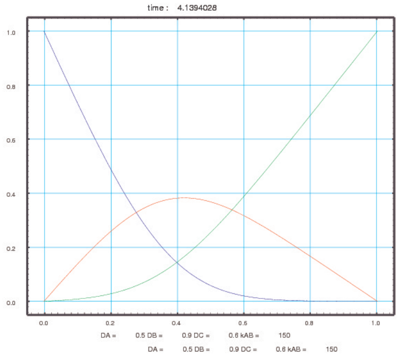

(c) $D_b = 0.9$

Figure 2.2: Effect of changing D_b. $D_a = 0.5$, $D_c = 0.6$, $k_{AB} = 150$, Initial conditions as shown in Figure 2.1

Table 2.1 shows $\max_{x \in [L,U]} C(x)$ in the steady state as a function of D_b.

Table 2.1: Maximum of $C(x)$ as function of D_b

D_b	$\max_{x \in [L,U]} C(x)$
0.1	0.110739424
0.5	0.309249483
0.9	0.382674985

Next numerical test investigates the effects of changing D_c on the steady state solution, keeping all other parameters constant. Figure 2.3 gives the initial concentration profiles of A, B and C at $t = 0$. Figure 4 shows the steady state solutions for different D_cs.

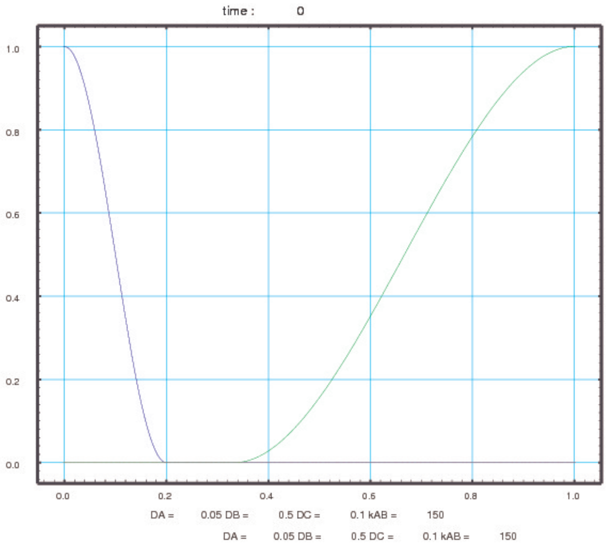

Figure 2.3: Concentration profiles at $t = 0$. $A(x, 0) = f_1(x)$, $B(x, 0) = g_3(x)$, $C(x, 0) = 0$.

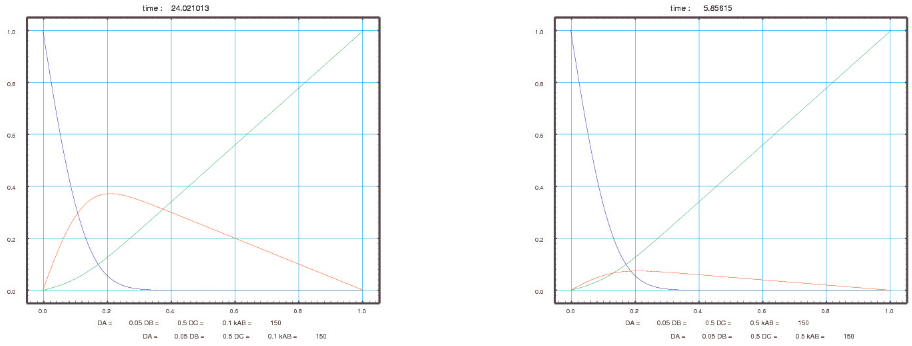

(a) $D_c = 0.1$

(b) $D_c = 0.5$

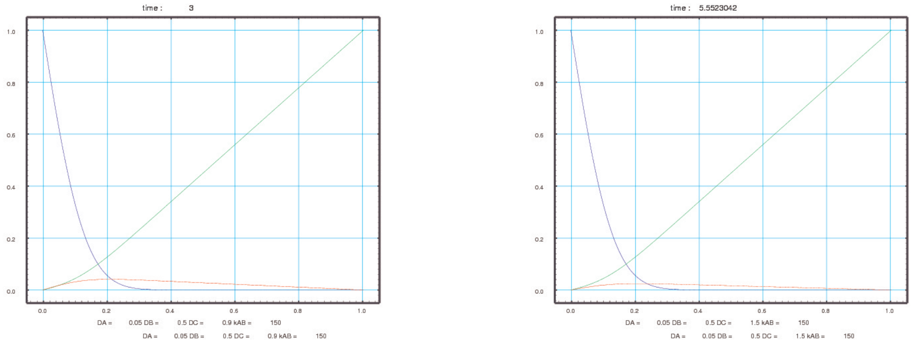

(c) $D_c = 0.9$

(d) $D_c = 1.5$

Figure 2.4: Effect of changing D_c. $D_a = 0.05$, $D_b = 0.5$, $k_{AB} = 150$, Initial conditions as shown in Figure 2.3

Table 2.2 shows $\max\limits_{x\in[L,U]} C(x)$ in the steady state as a function of D_c.

Table 2.2: Maximum of $C(x)$ as function D_c

D_c	$\max\limits_{x\in[L,U]} C$
0.1	0.371905875
0.5	0.074381175
0.9	0.041322932
1.5	0.024793725

Next we investigate the effect of changing the homogeneous reaction constant k_{AB} on the steady state solution, keeping other parameters constant. Figure 2.5 shows the initial concentration profiles at $t = 0$. Figure 2.6 shows the steady state solutions for different k_{AB}s. Table 2.3 gives $\max\limits_{x\in[L,U]} C$ in the steady state as a function of k_{AB}. It also gives T_s as a function of k_{AB}, where T_s is the time required by the system to attain steady state.

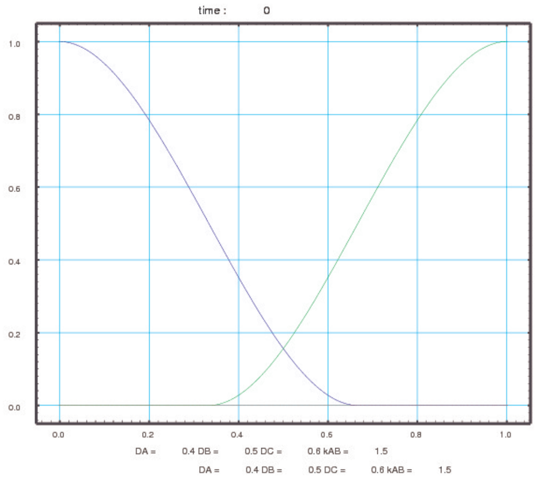

Figure 2.5: Concentration profiles at $t = 0$. $A(x, 0) = f_3(x)$, $B(x, 0) = g_3(x)$, $C(x, 0) = 0$.

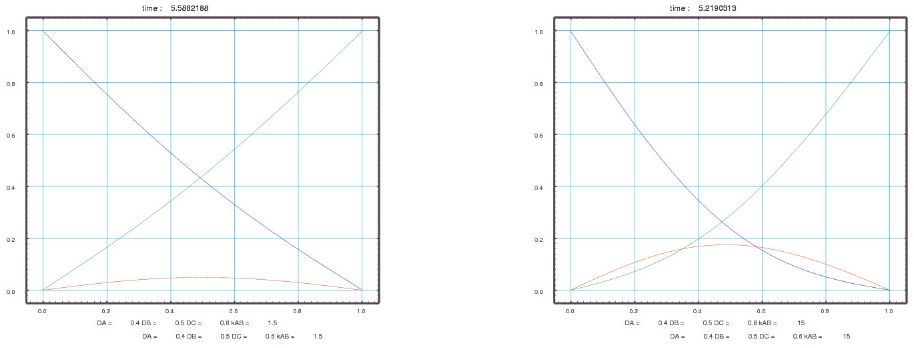

(a) $k_{AB} = 1.5$

(b) $k_{AB} = 15$

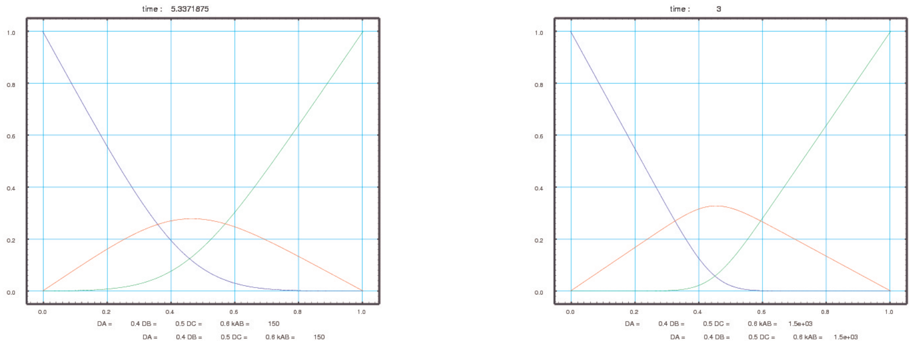

(c) $k_{AB} = 150$

(d) $k_{AB} = 1500$

Figure 2.6: Effect of changing k_{AB}. $D_a = 0.4$, $D_b = 0.5$, $D_c = 0.6$, Initial conditions as shown in Figure 2.5.

Table 2.3: Maximum of $C(x)$ and T_s as a function of k_{AB}

k_{AB}	$\max\limits_{x \in [L,U]} C(x)$	T_s
1.5	0.049561224	5.58828125
15	0.175430869	5.21909375
150	0.278307273	5.33725
1500	0.327634034	3.000041667

Lastly we investigate the effects of different initial conditions on the steady state solution and T_s. Figure 2.7 to Figure 2.9 show different initial concentration profiles and corresponding steady state solutions.

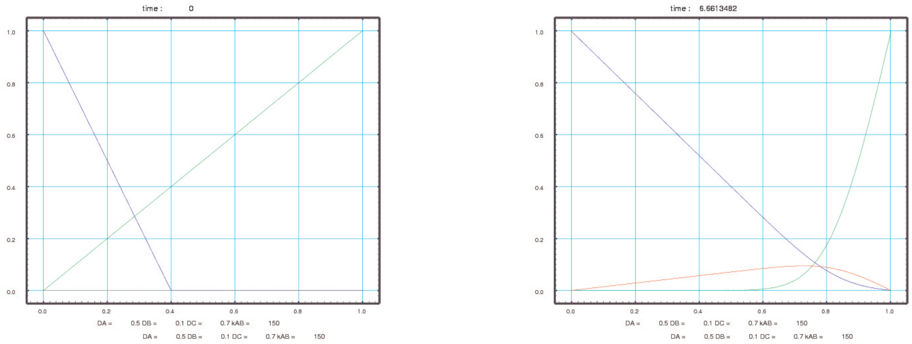

(a) $A(x,0) = f_5(x)$, $B(x,0) = g_2(x)$, $C(x,0) = 0$

(b) Steady State

Figure 2.7: $D_a = 0.5$, $D_b = 0.1$, $D_c = 0.7$, $k_{AB} = 150$

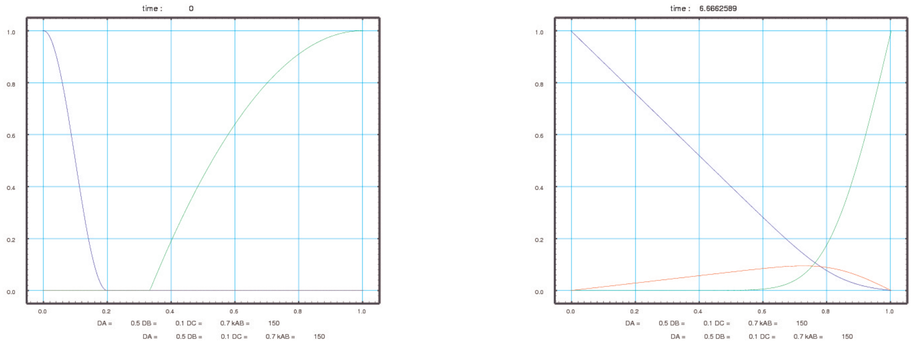

(a) $A(x,0) = f_1(x)$, $B(x,0) = g_4(x)$, $C(x,0) = 0$

(b) Steady State

Figure 2.8: $D_a = 0.5$, $D_b = 0.1$, $D_c = 0.7$, $k_{AB} = 150$

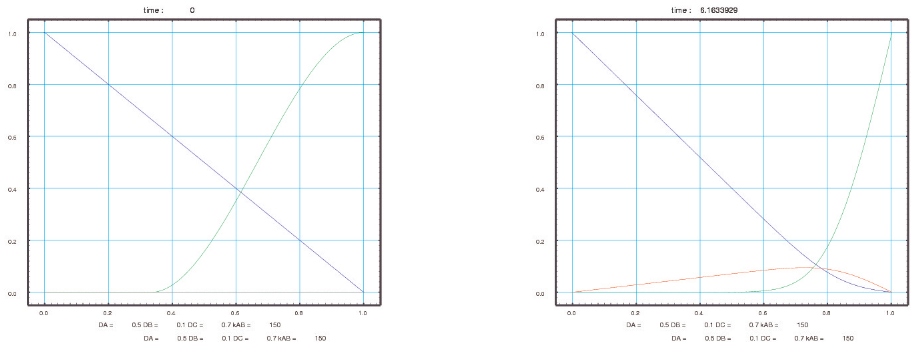

(a) $A(x,0) = f_2(x)$, $B(x,0) = g_3(x)$, $C(x,0) = 0$

(b) Steady State

Figure 2.9: $D_a = 0.5$, $D_b = 0.1$, $D_c = 0.7$, $k_{AB} = 150$

As seen from Figure 2.7 to Figure 2.9, the steady state solutions are not affected by the initial concentration profiles. However, the time required to attain steady state was affected and is recorded in Table 2.4.

Table 2.4: T_s against Initial Conditions

Initial Conditions	T_s
$f_5(x)$, $g_2(x)$	6.661392857
$f_1(x)$, $g_4(x)$	6.666303571
$f_2(x)$, $g_3(x)$	6.1634375

2.1.3 Summary of the steady state solutions

The purpose of the numerical tests presented in the previous section was to investigate the effects of different parameters on the steady state solutions of the system in one spatial dimension. Although the precipitation term is absent, it can be seen that precipitation is feasible only for a certain range of parameters which control $max_{x\in\Omega}C$. In higher spatial dimensions where precipitation term is present, precipitation cannot occur if $C_{eq} >> max_{x \in \Omega} C$, where C_{eq} represents equilibrium concentration. This is a consequence of supersaturation theory which posits that precipitation occurs when the concentration of the precipitating chemical component is more than a threshold concentration. When it is feasible, the direction in which the crystal mass keeps growing will be controlled by the points at which $max_{x \in \Omega} C$ is attained, which in turn are controlled by D_a, D_b, D_c and k_{AB}. To this end, it can be observed that the point at which $max_{x \in \Omega} C$ occurs is controlled by $\frac{D_a}{D_b}$. The ratio also has a significant effect on $max_{x \in \Omega} C$. On the other hand $\frac{D_a}{D_c}$ only controls $max_{x \in \Omega} C$, and not the point at which maximum occurs. Similarly, k_{AB} affects only $max_{x \in \Omega} C$, and not the point at which maximum occurs. However, k_{AB} has a significant effect on T_s, with T_s being reduced as k_{AB} increases. The exact mathematical relationship between k_{AB} and T_s could not be determined from the present numerical tests. The initial concentration profiles have a negligible effect on steady state solution as well as T_s.

2.2 Reaction-Diffusion Front

In the last section, we investigated the steady state solutions for the chemical reaction $A + B \rightarrow C$. The stoichiometric coefficients were assumed to be all 1's. In this section, we modify the experimental setup a little bit. Instead of considering a long thin tube with finite length, we consider the tube having no restrictions on the length. We also change the chemical reaction to $nA + mB \rightarrow C$. We assume that at time $t = 0$, the reactant are sharply separated from each other at point $x = 0$. The concentration of A (for all $x < 0$) is a_0 and that of B (for all $x > 0$) is b_0. Initially there is no component C present in the domain and the reaction starts at time $t = 0$. The experimental setup is illustrated in the following figure.

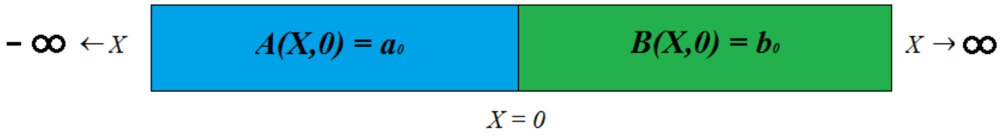

Figure 2.10: Experimental Setup.

Reactants A and B start to react and diffuse at time $t = 0$, and a zone is formed in which concentrations of A and B are relatively depleted. This zone is called *depletion zone*. Inside the depletion zone, there is a narrower zone called the *reaction front*. Concentration of the product C is at it's highest levels inside the reaction front. The concentration profiles of A, B and C at some arbitrary time t are similar to what is shown in the following figure. Precise definitions concerning reaction front and the depletion zone will be given later.

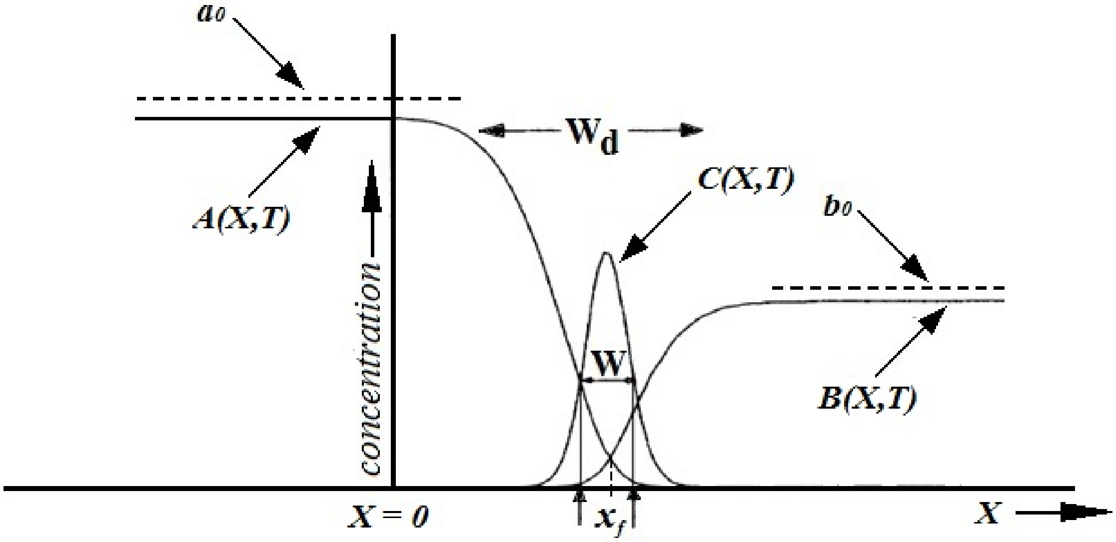

Figure 2.11: Concentrations of A, B and C at some arbitrary time t. The stoichiometric coefficients (n, m) are assumed to be $(1, 1)$. Concentration profiles for other values of the coefficients (n, m) are qualitatively the same. (This figure is adopted from a similar figure by Galfi and Racz [24])

2.2.1 Mathematical Model and Definitions

Reaction-Diffusion system given by the equations 2.4 to 2.6 describes the evolution of concentrations for the chemical reaction $A + B \longrightarrow C$, in which all three chemical species are assumed to diffuse within the domain. In this section, we generalize the mathematical model to include reactions of type $nA + mB \longrightarrow C$.

However, we assume that the product C does not diffuse in the domain. The diffusivities of A and B are given by D_a and D_b respectively. For the sake of brevity, we denote the homogeneous reaction constant by k instead of k_{AB}. As we have already mentioned, the domain in which the reaction takes place is (effectively) one-dimensional and has no restriction on its length. The two reactants A and B are assumed to be separated initially at $X = 0$. For the remainder of this section, we will follow the convention that, 1. the symbols X and T will denote real length and time, and the symbols x and t will denote normalized (dimensionless) length and time, 2. symbols $A(.)$, $B(.)$ and $C(.)$ will denote real concentrations, and the symbols $a(.)$, $b(.)$ and $c(.)$ will denote normalized (dimensionless) concentrations, 3. the symbols a_0 and b_0 will denote real initial concentrations of A and B in the domain. (Note that with these conventions, one can interprete a quantity like $A(x, T)$ to mean the real concentration of reactant A at a point whose normalized space coordinate is x and at real time T. However, we will have no use of such quantities. We will simply use either all real quantities or all dimensionless quantities.)

With the conventions above, the equations for the RDP in Figure 2.10 are given as follows:

$$\begin{aligned}
\frac{\partial A(X,T)}{\partial T} &= D_a \frac{\partial^2 A(X,T)}{\partial X^2} - knA^n(X,T)B^m(X,T) && (2.24)\\
\frac{\partial B(X,T)}{\partial T} &= D_b \frac{\partial^2 B(X,T)}{\partial X^2} - kmA^n(X,T)B^m(X,T) && (2.25)\\
\frac{\partial C(X,T)}{\partial T} &= kA^n(X,T)B^m(X,T) && (2.26)
\end{aligned}$$

The initial conditions are given as:

$$\begin{aligned}
A(X,0) &= a_0\theta(-X) && (2.27)\\
B(X,0) &= b_0\theta(X) && (2.28)\\
C(X,0) &= 0 && (2.29)
\end{aligned}$$

where $\theta(.)$ represents the Heaviside Step Function.

We now give some definitions concerning the RDP described by the Figures 2.10, 2.11 and the equations (2.24) to (2.26).

1. Reaction Front / Reaction Zone is defined as the region where the rate of production of C is the highest compared to rest of the domain. Typically, the reaction front is not stationary and keeps moving in a direction determined by other parameters of the system (like the diffusivities).

***2.* Center of Reaction Front** has been variably defined in the literature as the point at which the production rate of C is the highest or as the point at which $mA(X,T) = nB(X,T)$. We adopt the later definition. We also mention that these two points may not necessarily coincide. Galfi and Racz [24] have proved that for a first order reaction ($n = 1$, $m = 1$), both these points coincide in the large time limit. Since the reaction front moves with time, the center of reaction front is also a function of time, and will be denoted by $x_f(t)$ (in the dimensionless equations).

***3.* Width of the Reaction Front (w)** is defined as the second moment of the rate of production $r(x,t) = ka^n(x,t)b^m(x,t)$.

$$w^2(t) = \frac{\int\limits_{-\infty}^{\infty} (x - x_f(t))^2 r(x,t)dx}{\int\limits_{-\infty}^{\infty} r(x,t)dx} \tag{2.30}$$

***4.* Depletion Zone (W_d)** is defined as the region where the product $a^n(x,t)b^m(x,t)$ is significantly lower than $a_0^n b_0^m$.

***5.* Order of Reaction** is defined as the ordered pair of stoichiometric coefficients (n,m) for the chemical reaction $nA + mB \longrightarrow C$.

2.2.2 Dimensionless Equations

Following derivations for the dimensionless equations are adopted from Galfi and Racz [24] and Magnin [25]. Non-dimensionaliztion is done for the system of RDEs (2.24) to (2.26) along with the ICs (2.27) to (2.29), which describe the RDP for chemical reaction $nA + mB \longrightarrow C$.

2.2.2.1 The case of equal diffusivities

We make a key assumption that $D_a = D_b = D$. (This assumption is extremely difficult to reproduce in a laboratory setting and is quite unrealistic. However, it makes mathematics more manageable and paves way for the case of arbitrary diffusivities). With this assumption, we introduce the characteristic length as $l := \sqrt{\frac{D}{k \cdot {a_0}^{n+m-1}}}$ and characteristic time as $\tau := \frac{1}{k \cdot {a_0}^{n+m-1}}$. We also introduce characteristic concentration to be a_0, and assume that D_a, D_b, k, a_0 and b_0 remain constant. We now introduce dimensionless length, time and concentration as $x := \frac{X}{l}$, $t := \frac{T}{\tau}$ and $a(x,t) := \frac{A(X,T)}{a_0}$, $b(x,t) := \frac{B(X,T)}{a_0}$, $c(x,t) := \frac{C(X,T)}{a_0}$. With this change of variables, the terms in the RDEs (2.24) to (2.26) can now be written as $\frac{\partial A}{\partial T} = k{a_0}^{n+m}\frac{\partial a}{\partial t}$; $\frac{\partial B}{\partial T} = k{a_0}^{n+m}\frac{\partial b}{\partial t}$; $\frac{\partial C}{\partial T} = k{a_0}^{n+m}\frac{\partial c}{\partial t}$; $\frac{\partial^2 A}{\partial X^2} = \frac{k{a_0}^{n+m}}{D}\frac{\partial^2 a}{\partial x^2}$; $\frac{\partial^2 B}{\partial X^2} = \frac{k{a_0}^{n+m}}{D}\frac{\partial^2 b}{\partial x^2}$; $knA^nB^m = kn{a_0}^{n+m}a^nb^m$; $kmA^nB^m = km{a_0}^{n+m}a^nb^m$ and $kA^nB^m = k{a_0}^{n+m}a^nb^m$, where A, B, C represent $A(X,T)$, $B(X,T)$, $C(X,T)$ respectively and a, b, c represent $a(x,t)$, $b(x,t)$, $c(x,t)$ respectively. Substituting these into RDEs (2.24) to (2.26) and the ICs (2.27) to (2.29) and cancelling common terms, we get the : following dimensionless RDS:

$$\frac{\partial a}{\partial t} = \frac{\partial^2 a}{\partial x^2} - na^nb^m \tag{2.31}$$

$$\frac{\partial b}{\partial t} = \frac{\partial^2 b}{\partial x^2} - ma^nb^m \tag{2.32}$$

$$\frac{\partial c}{\partial t} = a^nb^m \tag{2.33}$$

subject to the initial conditions

$$a(x,0) = \theta(-x) \tag{2.34}$$

$$b(x,0) = \frac{b_0}{a_0}\theta(x) \tag{2.35}$$

$$c(x,0) = 0 \tag{2.36}$$

For the dimensionless system, the domain is $\Omega = \{(x,t)|(x,t) \in \mathbb{R} \times [0,\infty)\}$. At this point we introdue a new function $u(x,t) := a(x,t) - \frac{n}{m}b(x,t)$. To understand the motivation behind this definition, recall the definition of the Center of Reaction Front, $x_f(t)$. (It is defined as the point where $ma(x,t) = nb(x,t)$). Thus $x_f(t)$ is precisely the point where $u(x,t) = 0$. To find an expression for $x_f(t)$, we will show that $u(x,t)$ satisfies the Diffusion equation over the whole real line. Thus it will become a pure initial value problem in one spatial dimension which can be solved using Fourier Transforms or Eigenvalue functions.

Multiply equation (2.32) by $\frac{n}{m}$ and subtract from equation(2.31). Thus we get

$$\frac{\partial}{\partial t}(a - \frac{n}{m}b) = \frac{\partial^2}{\partial x^2}(a - \frac{n}{m}b)$$

$$\Longrightarrow \quad \frac{\partial u}{\partial t} = \frac{\partial^2 u}{\partial x^2} \tag{2.37}$$

Define $q := \frac{b_0}{a_0}$. Then the initial conditions (2.34) and (2.35) for equation (2.37) are given by:

$$u(x,0) = \theta(-x) - \frac{n}{m} q \theta(x) \tag{2.38}$$

Now equation(2.37) along with the IC (2.38) becomes a pure initial value problem for the Diffusion Equation. It's solution is given by:

$$u(x,t) = \frac{1}{2}\left(\left(1 - \frac{n}{m}q\right) - \left(1 - \frac{n}{m}q\right) \cdot erf\left(\frac{x}{2\sqrt{t}}\right)\right) \tag{2.39}$$

where $erf(\cdot)$ represents the *error function.* At $x = x_f(t)$, $u(x,t) = 0$. Hence we get

$$x_f(t) = \sqrt{2D_f t} \tag{2.40}$$

where D_f is given by

$$D_f = 2\left(erf^{-1}\left(\frac{1 - \frac{n}{m}q}{1 + \frac{n}{m}q}\right)\right)^2 \tag{2.41}$$

where $erf^{-1}(\cdot)$ represents *inverse error function.*

We wish to emphasize the point that the movement of the center of reaction zone is proportional to the square root of time. This is to be expected since this form of relationship is the signature of a typical diffusion process. We wish to further emphasize the fact that the proportionality constant, $\sqrt{2D_f}$, is a function of n, m and q. This will be explored in greater details in the subsequent sections.

2.2.2.2 The case of arbitrary diffusivities

For the case of arbitrary diffusivities, we can no longer use the assumption that $D_a = D_b$. This assumption was a key factor in deriving equations (2.39), (2.40) and (2.41). Without this assumption, the mathematics quickly becomes untenable. To the best of our knowledge, no closed form expression for $x_f(t)$ exists for the case of arbitrary diffusivities. Thus we must resort to numerical solutions to study the movement of the reaction front.

In this section, we first derive dimensionless equations for the RDEs (2.24) to (2.26) along with the ICs (2.27) to (2.29). In the next section, we put forth a cojecture regarding $x_f(t)$. In the section on numerical results, we present numerical evidence in support of the conjecture.

For the case of arbitrary diffusivities, we can either choose D_a or D_b in place of D. We choose D_a and we introduce the characteristic length as $l := \sqrt{\frac{D_a}{k{a_0}^{n+m-1}}}$ and characteristic time as $\tau := \frac{1}{k{a_0}^{n+m-1}}$. We also introduce characteristic concentration to be a_0, and assume that D_a, D_b, k, a_0 and b_0 remain constant. We now introduce dimensionless length, time and concentration as $x := \frac{X}{l}$, $t := \frac{T}{\tau}$ and $a(x,t) := \frac{A(X,T)}{a_0}$, $b(x,t) := \frac{B(X,T)}{a_0}$, $c(x,t) := \frac{C(X,T)}{a_0}$. (Notice that these definitions are identical to the case of equal diffusivities except for the fact that we have used D_a instead of D). With this change of variables, the terms in the RDEs (2.24) to (2.26) can now be written as $\frac{\partial A}{\partial T} = k{a_0}^{n+m}\frac{\partial a}{\partial t}$; $\frac{\partial B}{\partial T} = k{a_0}^{n+m}\frac{\partial b}{\partial t}$; $\frac{\partial C}{\partial T} = k{a_0}^{n+m}\frac{\partial c}{\partial t}$; $\frac{\partial^2 A}{\partial X^2} = \frac{k{a_0}^{n+m}}{D_a}\frac{\partial^2 a}{\partial x^2}$; $\frac{\partial^2 B}{\partial X^2} = \frac{k{a_0}^{n+m}}{D_a}\frac{\partial^2 b}{\partial x^2}$; $knA^nB^m = kn{a_0}^{n+m}a^nb^m$; $kmA^nB^m = km{a_0}^{n+m}a^nb^m$ and $kA^nB^m = k{a_0}^{n+m}a^nb^m$, where A, B, C represent $A(X,T)$, $B(X,T)$, $C(X,T)$ respectively and a, b, c represent $a(x,t)$, $b(x,t)$, $c(x,t)$ respectively. Substituting these into RDEs (2.24) to (2.26) and the ICs (2.27) to (2.29) and cancelling common terms, we get the following dimensionless RDS:

$$\frac{\partial a}{\partial t} = \frac{\partial^2 a}{\partial x^2} - na^nb^m \tag{2.42}$$

$$\frac{\partial b}{\partial t} = \frac{D_b}{D_a}\frac{\partial^2 b}{\partial x^2} - ma^nb^m \tag{2.43}$$

$$\frac{\partial c}{\partial t} = a^nb^m \tag{2.44}$$

subject to the initial conditions

$$a(x,0) = \theta(-x) \tag{2.45}$$

$$b(x,0) = \frac{b_0}{a_0}\theta(x) \tag{2.46}$$

$$c(x,0) = 0 \tag{2.47}$$

As for the case of equal diffusivities, the domain is once again $\Omega = \{(x,t)|(x,t) \in \mathbb{R} \times [0,\infty)\}$. Unfortunately, due to the the coefficient $\frac{D_b}{D_a}$ in equation (2.43), it is not possible to carry out any simplifications similar to the previous case. As mentioned earlier, no closed form expression for $x_f(t)$ is currently known for the case of arbitrary diffusivities. However, observe that the process is diffusive. Thus we will put forward the following conjecture.

2.2.2.3 Conjecture for arbitrary diffusivities

Observe that for the case of equal diffusivities, $x_f(t) \propto \sqrt{t}$ and that the propotionality constant $\eta = \sqrt{2D_f}$ is a function of n, m and q. (D_f has been defined by equation (2.41)).

Based on these observations, we put forth the following conjecture: *"For the dimensionless reaction-diffusion system described by equations (2.42) to (2.44) along with the initial conditions (2.45) to (2.47), the position of the center of reaction-front at any time t is proportional to $\sqrt{t}$. Further, the constant of proportionality, η, is a function of $\frac{D_b}{D_a}$, n, m and q."* (i.e. $x_f(t) = \eta(\frac{D_b}{D_a}, n, m, q)\sqrt{t}$).

To the best of our knowledge, no known mathematical proof exists for this conjecture. Known results are all asymptotic in nature [30, 34]. Thus we present numerical evidence in support of this conjecture.

2.2.3 Numerical Results

Our goal in this section is to solve equations (2.42) to (2.44) numerically and to find the position of $x_f(t)$, thereby producing numerical evidence in support of the conjecture put forth in the last section.

We first apply the numerical method described below to the case of equal diffusivities to and compare the numerical solution to the analytical solution to establish the accuracy of the method. Next we carry out numerical tests to explain the initial "overshoots" and "undershoots" near $t = 0$. Once the accuracy of our method has been established, we then apply the method to the case of arbitrary diffusivities to show the numerical evidence in support of the conjecture. We carry out the numerical tests for $(n, m) = (1, 1)$, $(1, 2)$, $(2, 1)$ and $(2, 2)$. In each case, we change the values of $\frac{D_b}{D_a}$ and q in uniform small intervals. The numerical method is described below.

We use Crank-Nicolson method to solve Eqn. (2.42) and (2.43). Discretization is given as follows:

$$\frac{a_j^{(k+1)} - a_j^{(k)}}{\Delta t} = \frac{1}{2}\left(\frac{a_{j-1}^{(k+1)} - 2a_j^{(k+1)} + a_{j+1}^{(k+1)}}{\Delta x^2} + \frac{a_{j-1}^{(k)} - 2a_j^{(k)} + a_{j+1}^{(k)}}{\Delta x^2}\right) - n(a_j^{(k)})^n(b_j^{(k)})^m \tag{2.48}$$

$$\frac{b_j^{(k+1)} - b_j^{(k)}}{\Delta t} = \frac{1}{2}\frac{D_b}{D_a}\left(\frac{b_{j-1}^{(k+1)} - 2b_j^{(k+1)} + b_{j+1}^{(k+1)}}{\Delta x^2} + \frac{b_{j-1}^{(k)} - 2b_j^{(k)} + b_{j+1}^{(k)}}{\Delta x^2}\right) - m(a_j^{(k)})^n(b_j^{(k)})^m \tag{2.49}$$

Here the subscript j represents spatial index and the superscript (k) represents time step. For the sake of completeness, we discretize equation (2.44) using the Forward Euler method. Forward Euler can be unstable and typically only first order. However we draw attention to the fact that our main interest is in studying the behavior of the center of reaction zone $x_f(t)$ which depends only on $a(x,t)$ and $b(x,t)$. Since equation (2.44) is decoupled from equation (2.42) and (2.43), consistency and stability of it's numerical solution will have no effect on the other two. It has been solved only for the sake of completeness. The discretization is given as follows:

$$\frac{c_j^{(k+1)} - c_j^{(k)}}{\Delta t} = (a_j^{(k)})^n(b_j^{(k)})^m \tag{2.50}$$

Notice that the original problem is an Initial Value Problem. So ideally j runs through all non-negative integers. However, due to the finite memory constraints of any computing platform, we restrict the computational domain to $[-1,1]$ and let j run through 0,1,...,M where $2/\Delta x = M$. Since the left and right boundaries are reasonably far from the initial reaction zone, it is also reasonable to approximate the boundary conditions as follows:

$$\left.\frac{\partial a(x,t)}{\partial x}\right|_{x=-1} = \left.\frac{\partial a(x,t)}{\partial x}\right|_{x=1} = 0 \tag{2.51}$$

$$\left.\frac{\partial b(x,t)}{\partial x}\right|_{x=-1} = \left.\frac{\partial b(x,t)}{\partial x}\right|_{x=1} = 0 \tag{2.52}$$

We implement these boundary conditions numerically as follows:

$$a_0^{(k+1)} = a_1^{(k+1)}, \qquad a_M^{(k+1)} = a_{M-1}^{(k+1)} \tag{2.53}$$

$$b_0^{(k+1)} = b_1^{(k+1)}, \qquad b_M^{(k+1)} = b_{M-1}^{(k+1)} \tag{2.54}$$

We note that the numerical boundary conditions can lead to only first order consistency at the boundary while Crank-Nicolson is expected to produce second order accuracy elsewhere in the computational domain. We overcome this problem by terminating the run as soon as diffusion process reaches the boundary. In particular, we terminate the code run as soon as any of $|a_0^{(k)} - a_1^{(k)}|, |a_M^{(k)} - a_{M-1}^{(k)}|, |b_0^{(k)} - b_1^{(k)}|, |b_M^{(k)} - b_{M-1}^{(k)}|$ is greater than $O(\Delta x^2)$.

To detect the position of the center of reaction zone $x_f(t)$, we use linear interpolation between the grid points $x_0, x_1, ..., x_M$ at every time step. In particular,at every time step k, we find out the index $i \in \{0, 1, 2, ..., M\}$ such that $(a_i^{(k)} - \frac{n}{m} b_i^{(k)})(a_{i+1}^{(k)} - \frac{n}{m} b_{i+1}^{(k)}) \leq 0$. Then we find out the location $x_f(t)$ by solving the two linear equations $\frac{y - a_i^{(k)}}{x - x_i} = \frac{a_{i+1}^{(k)} - a_i^{(k)}}{x_{i+1} - x_i}$ and $\frac{y - \frac{n}{m} b_i^{(k)}}{x - x_i} = \frac{n}{m} \frac{b_{i+1}^{(k)} - b_i^{(k)}}{x_{i+1} - x_i}$.

2.2.3.1 Numerical Results for $D_b/D_a = 1$ and $(n, m) = (1, 1)$

As discussed in the previous sections, the analytical expression for $x_f(t)$ in this case is given by $x_f(t) = \sqrt{2D_f t}$ where $erf\left(\sqrt{\frac{D_f}{2}}\right) = \frac{1-q}{1+q}$. In this section we compare the numerical results with analytical results and show that the numerical method described above indeed gives accurate results. All numerical tests have been carried out with the *FronTier* software library.

We begin by showing the numerical solutions for species A, B and C.

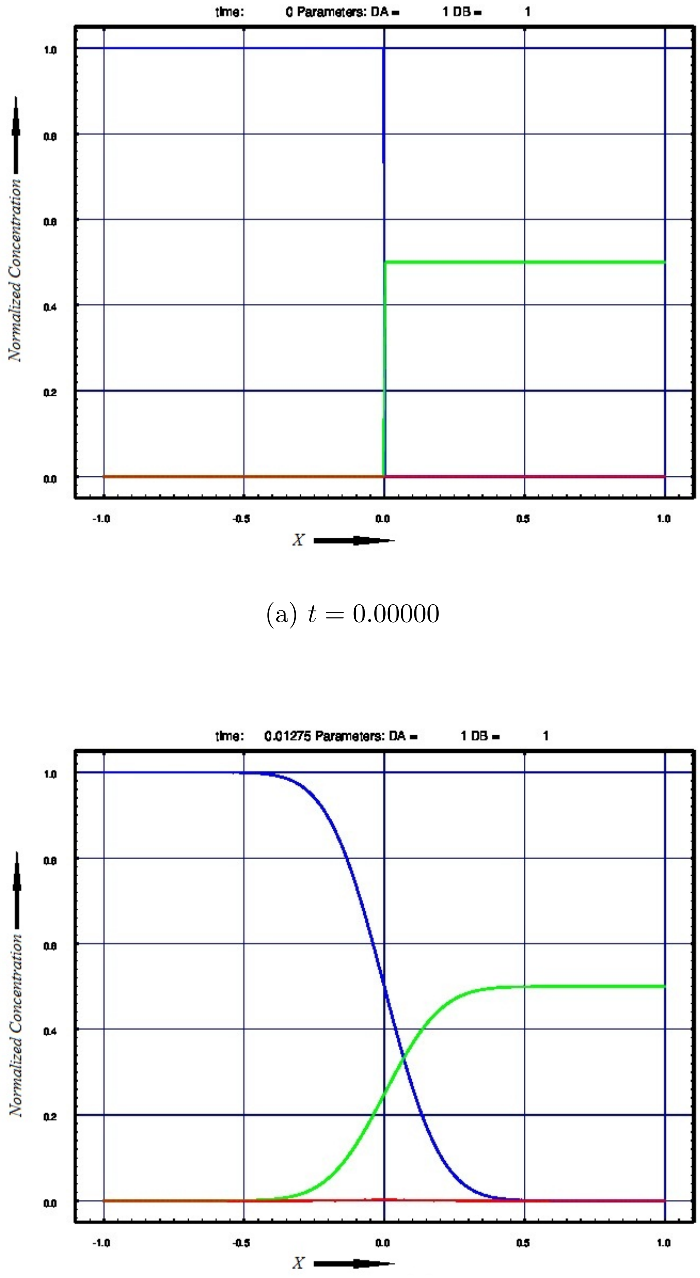

(a) $t = 0.00000$

(b) $t = 0.01275$

Figure 2.12: Numerical solutions for $q = 0.5$. *(continued on next page)*

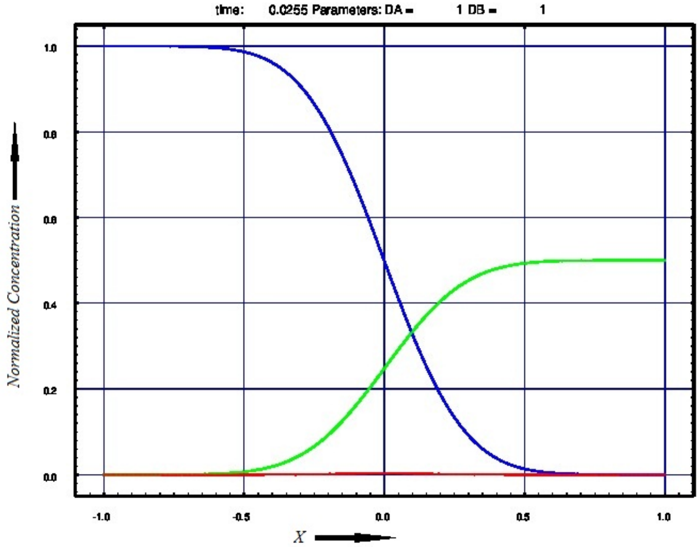

(c) $t = 0.02550$

Figure 2.12: Numerical solutions for $q = 0.5$. Blue line represents Normalized Concentration of species A, Green that of B and Red that of product C.

It can be seen that the numrical solutions match the expected shape of the concentration profiles of all three species. Next we verify that the numerical method gives the position of the center of reaction-diffusion zone correct upto second order. In the next figure, we show the numerical results for the theoretical $x_f(t)$ and numerical $x_f(t)$ vs. time t for various q's. In the graphs which follow, q changes from 0.1 to 1.0 in steps of 0.1 as one moves from the topmost branch of the graph to the lowest branch.

From Fig.2.13, it can be seen that as t increases, numerical $x_f(t)$ indeed aproaches theoretical $x_f(t)$ for every q. To further investigate the convergence of nuerical method, we present the same numerical results as $x_f(t)/\sqrt{t}$ vs. time t. Fig.2.14 indicates that $x_f(t)/\sqrt{t}$ indeed approaches a constant as time t increases.

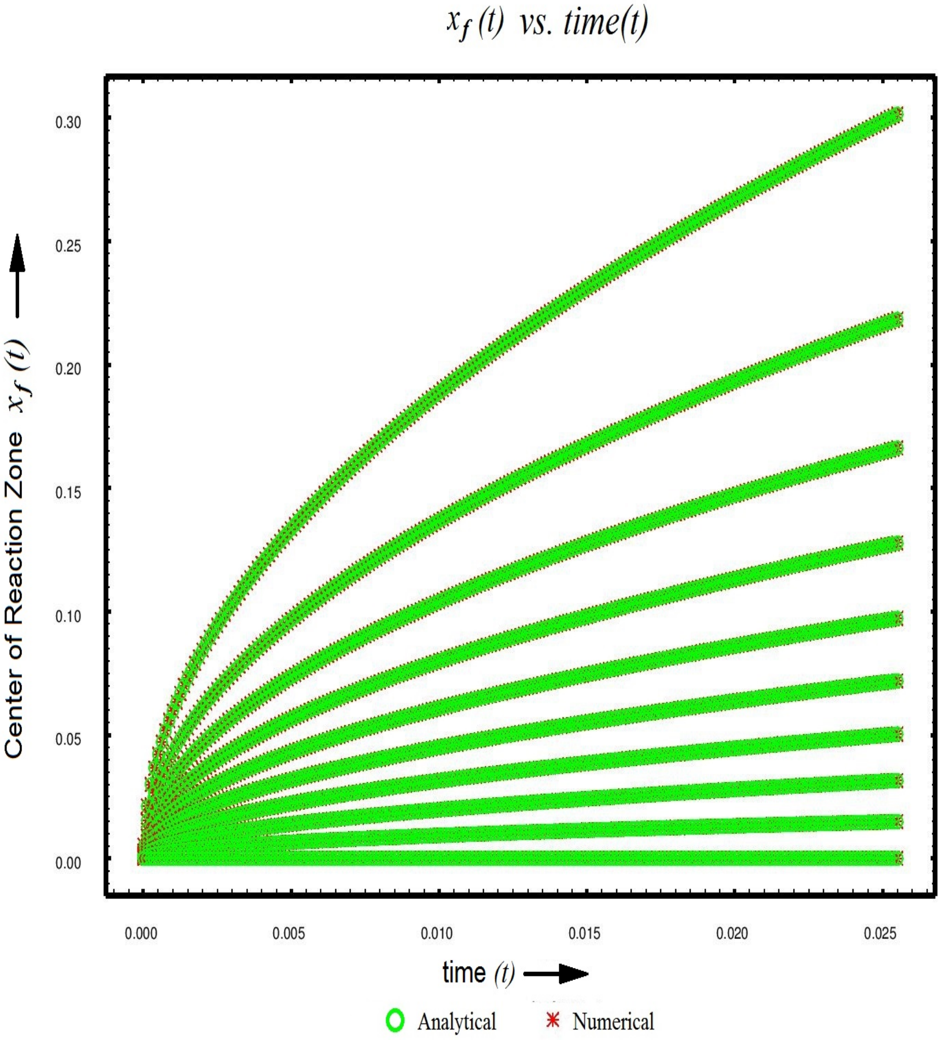

Figure 2.13: Graphical results for second order accuracy of the numerical method. Theoretical position of the center of reaction zone is given by $x_f(t) = 2erf^{-1}\left(\frac{1-q}{1+q}\right)\sqrt{t}$.

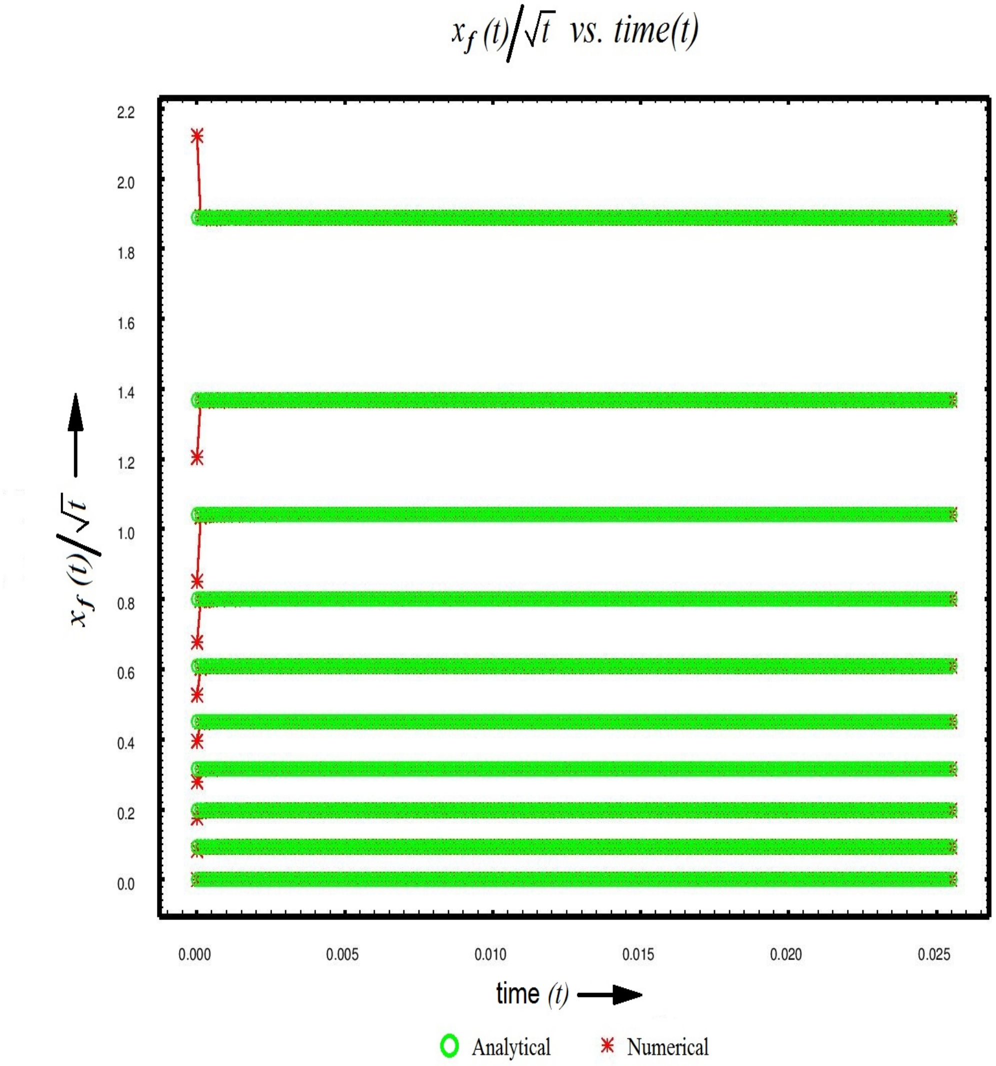

Figure 2.14: Graphical results for $x_f(t)/\sqrt{t}$ vs t for different q's.

Notice that in Fig.2.14, there is a spike and small oscillatory behaviour near $t = 0$ for most of the q's. This can be explained by the fact that the grid points are finite in number and hence not dense in the computational domain. Hence the initial conditions (Heaviside Step Function) cannot be realized perfectly on any computational grid on a computer. This fact is illustrated in Fig.2.15.

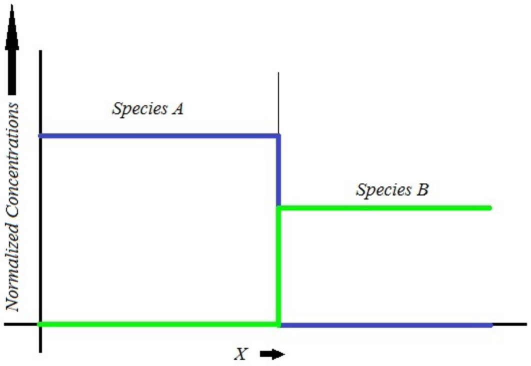

(a) Heaviside Step Function

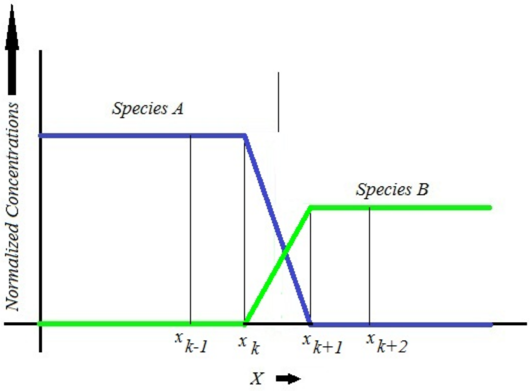

(b) Numerical Implementation

Figure 2.15: Implementation of Heaviside Step Function on a finite compuational grid

This fact is further verified by changing the grid-size. Next figure shows the effects of grid-size on the convergence of $x_f(t)/\sqrt{t}$.

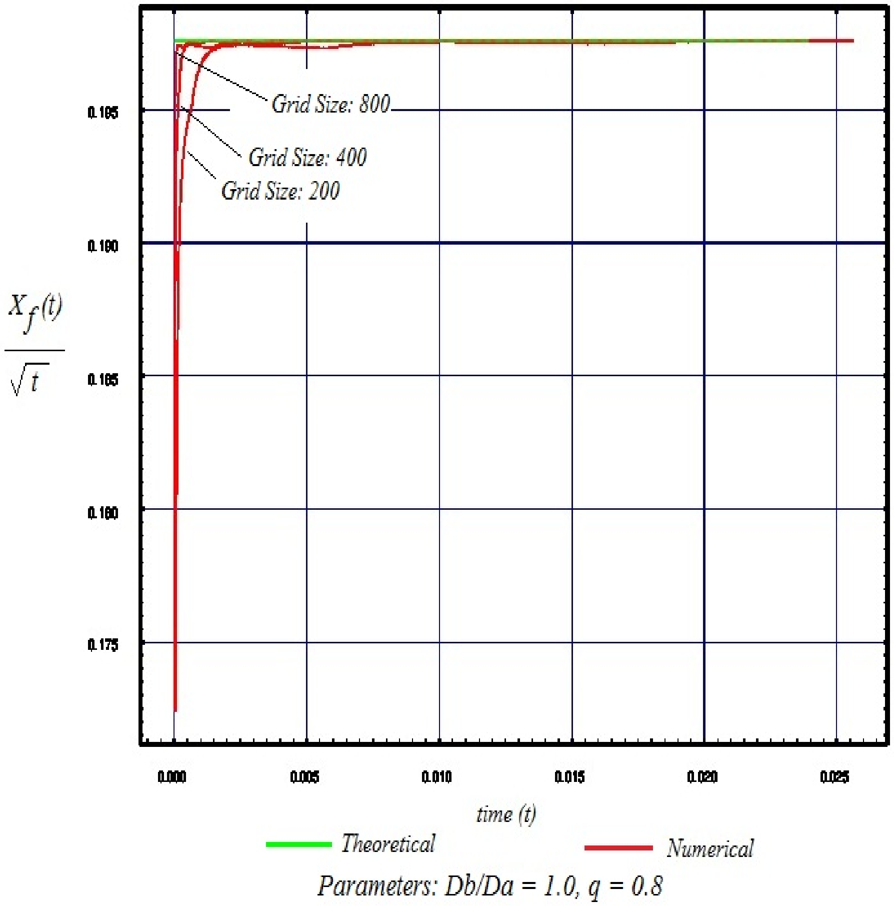

Figure 2.16: $x_f(t)/\sqrt{t}$ vs t for varying grid size.

It can be seen from Fig.2.16 that as the grid is refined, $x_f(t)/\sqrt{t}$ attains it's theoretical value at earlier time.

2.2.3.2 Numerical Results for $D_b/D_a \neq 1$ and $(n, m) = (1, 1)$

In the previous section, we have presented enough numerical evidence to show that the numerical method applied indeed gives results that match with theoretical results. In this section, we proceed to the case of $D_b/D_a \neq 1$. In this case, no closed form analytical expression is available for $x_f(t)$. Hence, we will provide numerical verification that $x_f(t)$ is indeed proportional to $\sqrt{t}$, and that the constant of proportionality η is a function of D_b/D_a and q. We present our numerical results for $D_b/D_a = 0.2, 0.4, 0.6$ and 0.8. Fig.2.17(a), Fig.2.18(a), Fig.2.19(a) and Fig.2.20(a) present the numerical results for $x_f(t)$ vs. t. Fig.2.17(b), Fig.2.18(b), Fig.2.19(b) and Fig.2.20(b) present the same results for $x_f(t)/\sqrt{t}$ vs. t. As mentioned previously, q changes from 0.1 to 1.0 in the steps of 0.1 as one moves from the topmost branch of the graph to the lowest branch.

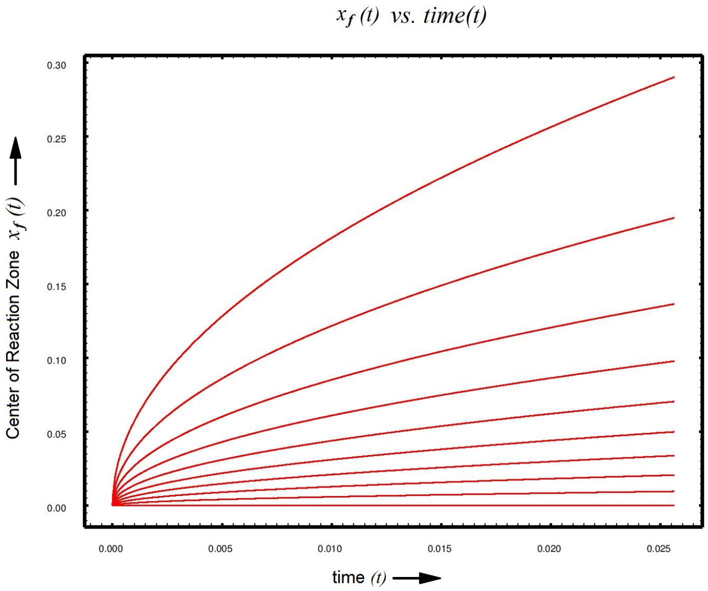

(a) $x_f(t)$ vs. t

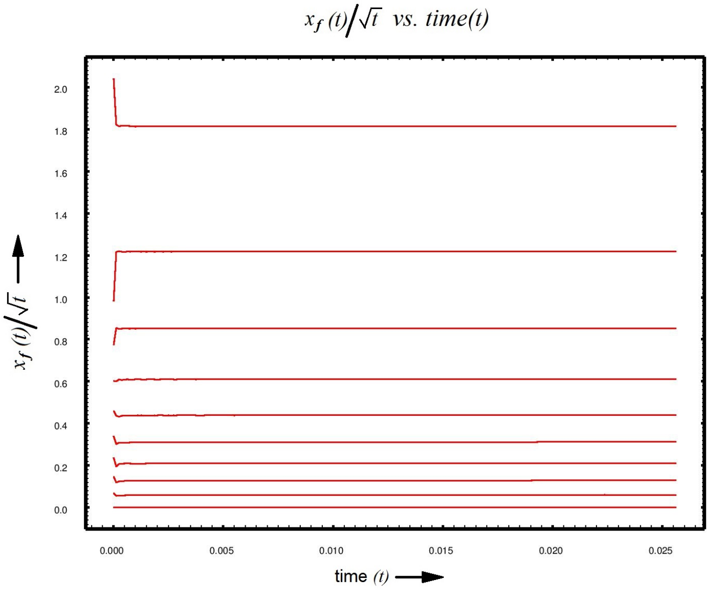

(b) $x_f(t)/\sqrt{t}$ vs. t

Figure 2.17: Center of Reaction Zone for $D_b/D_a = 0.2$ and $(n, m) = (1, 1)$

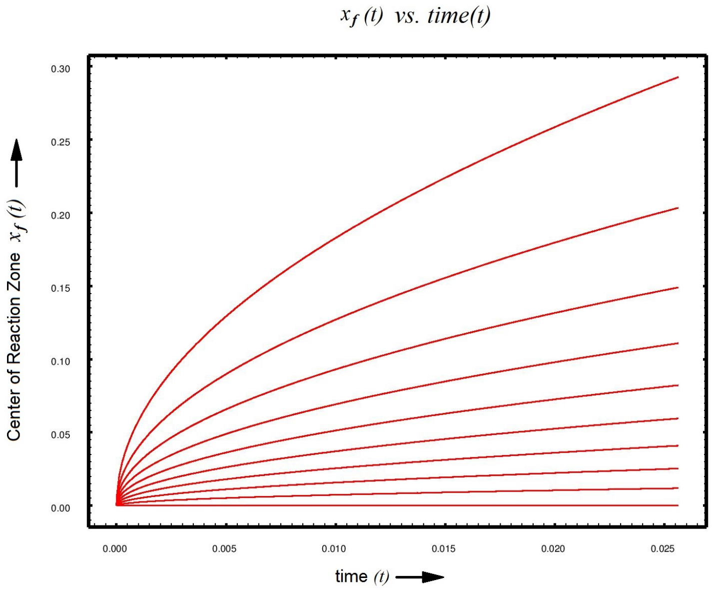

(a) $x_f(t)$ vs. t

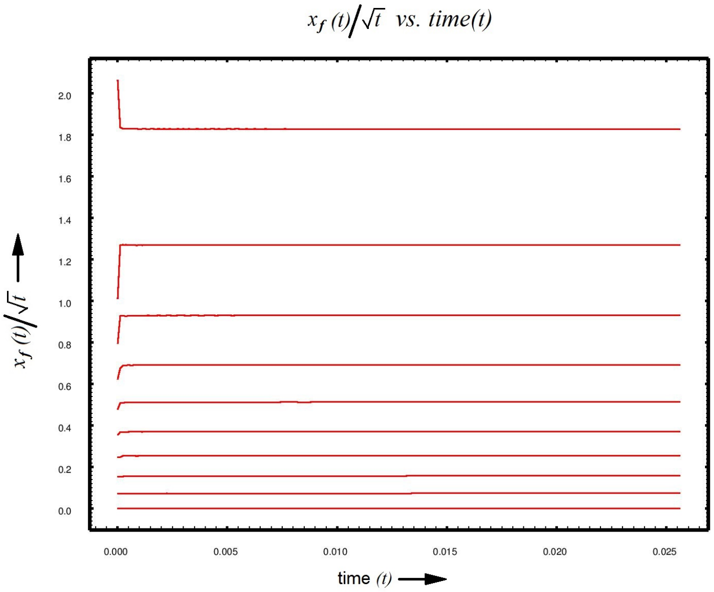

(b) $x_f(t)/\sqrt{t}$ vs. t

Figure 2.18: Center of Reaction Zone for $D_b/D_a = 0.4$ and $(n, m) = (1, 1)$

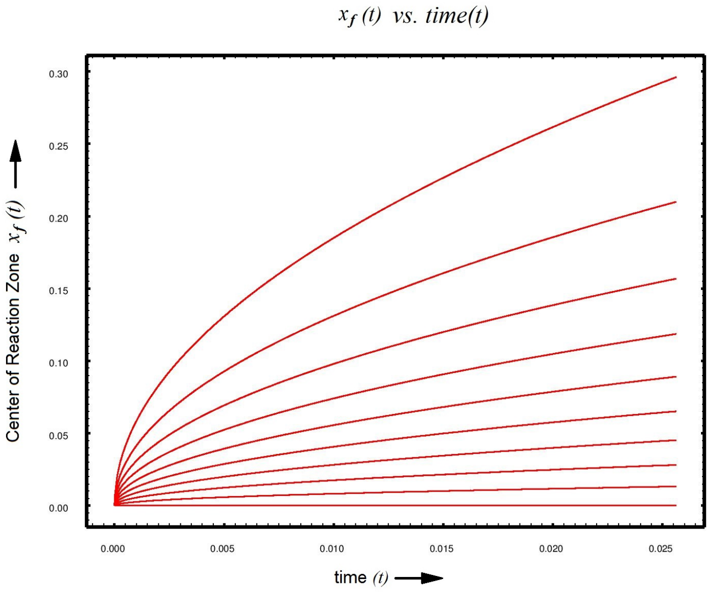

(a) $x_f(t)$ vs. t

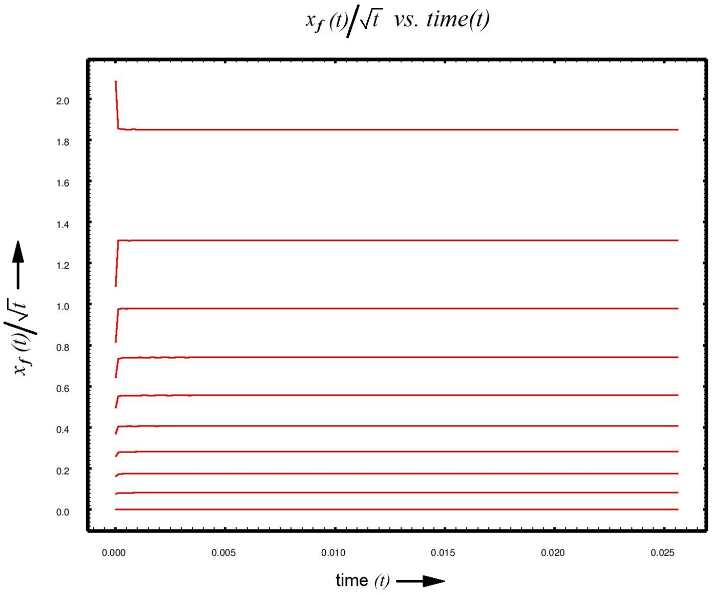

(b) $x_f(t)/\sqrt{t}$ vs. t

Figure 2.19: Center of Reaction Zone for $D_b/D_a = 0.6$ and $(n, m) = (1, 1)$

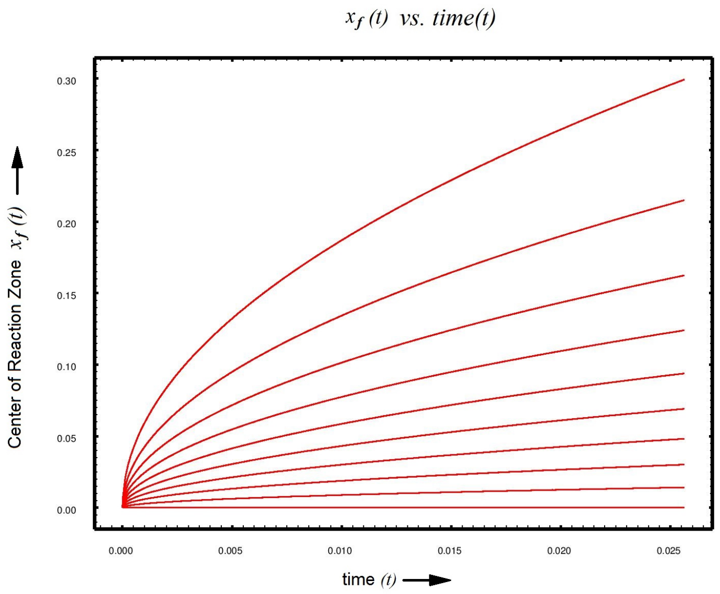

(a) $x_f(t)$ vs. t

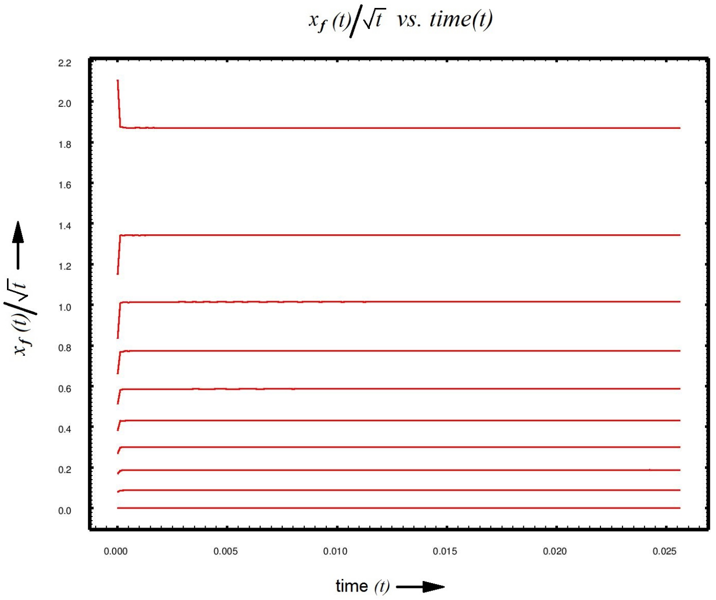

(b) $x_f(t)/\sqrt{t}$ vs. t

Figure 2.20: Center of Reaction Zone for $D_b/D_a = 0.8$ and $(n, m) = (1, 1)$

Thus, the numerical results presented in this section indeed verify the fact that $x_f(t) \propto \eta\big(D_b/D_a, n, m, q\big)\sqrt{t}$ for $(n, m) = (1, 1)$.

Next we present similar results for higher order reactions, $(n, m) = (1, 2), (2, 1)$ and $(2, 2)$. There is no qualitative difference in the results. The only difference is the specific numerical values of concentration profiles, reaction zone position etc.

2.2.3.3 Numerical Results for $D_b/D_a = 1$ and $(n, m) = (1, 2)$

As in previous section, we first present the comparison between theoretical and numerical results when $D_b/D_a = 1$. As mentioned previously, analytical results are available in this case only. q changes from 0.1 to 1.0 in the steps of 0.1 as one moves from the topmost branch of the graph to the lowest branch.

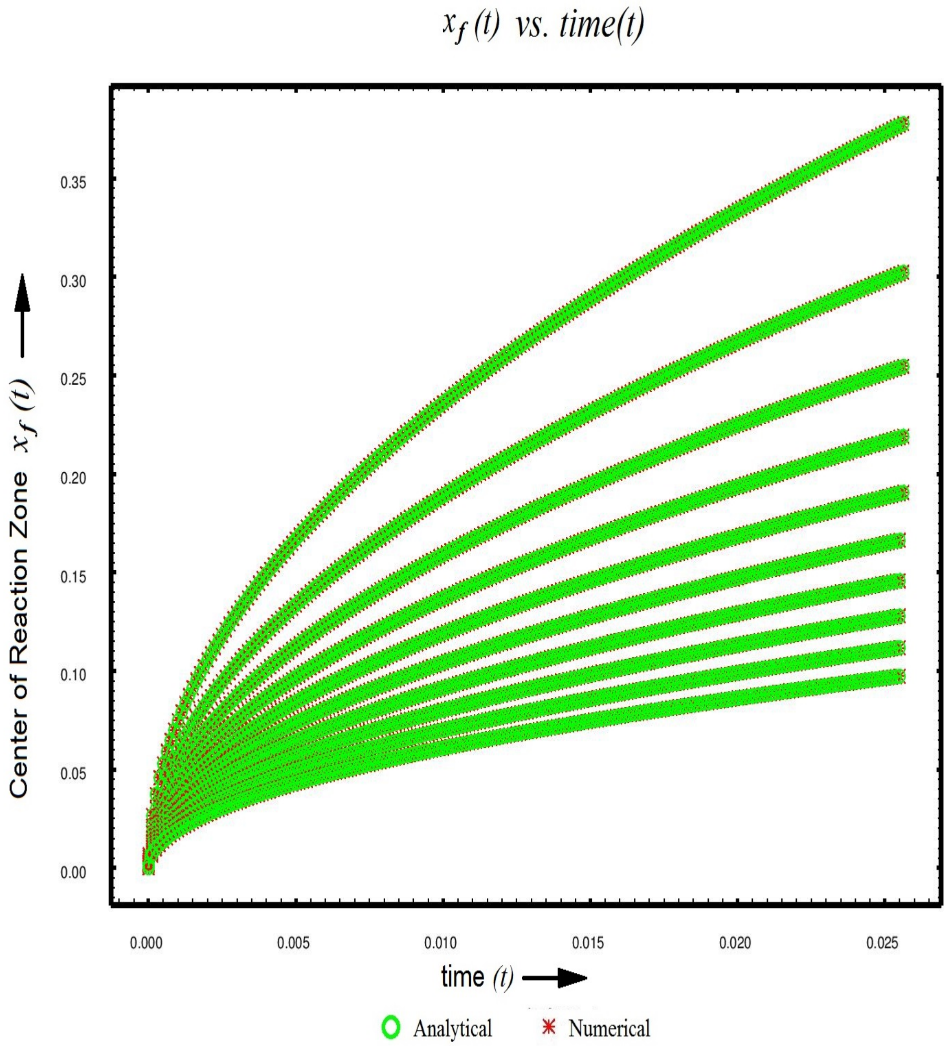

Figure 2.21: Graphical results for $(n, m) = (1, 2)$ Theoretical position of the center of reaction zone is given by $x_f(t) = 2erf^{-1}\big(\frac{1-\frac{1}{2}q}{1+\frac{1}{2}q}\big)\sqrt{t}$.

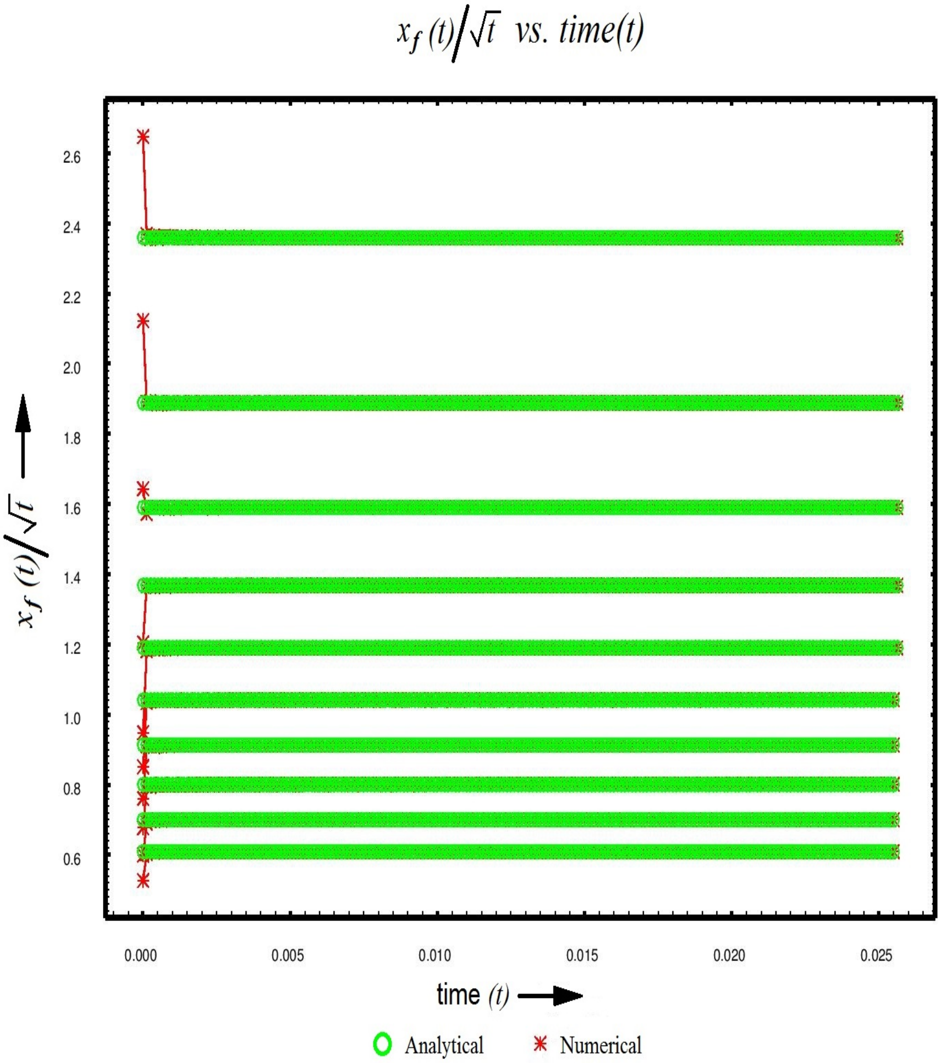

Figure 2.22: Graphical results for $x_f(t)/\sqrt{t}$ vs t for different q's.

These results show that the analytical and numerical results match with each other. Next we present the results for $D_b/D_a \neq 1$.

2.2.3.4 Numerical Results for $D_b/D_a \neq 1$ and $(n, m) = (1, 2)$

We present the numerical results for $D_b/D_a = 0.2, 0.4, 0.6$ and 0.8. q changes from 0.1 to 1.0 in the steps of 0.1 as one moves from the topmost branch of the graph to the lowest branch.

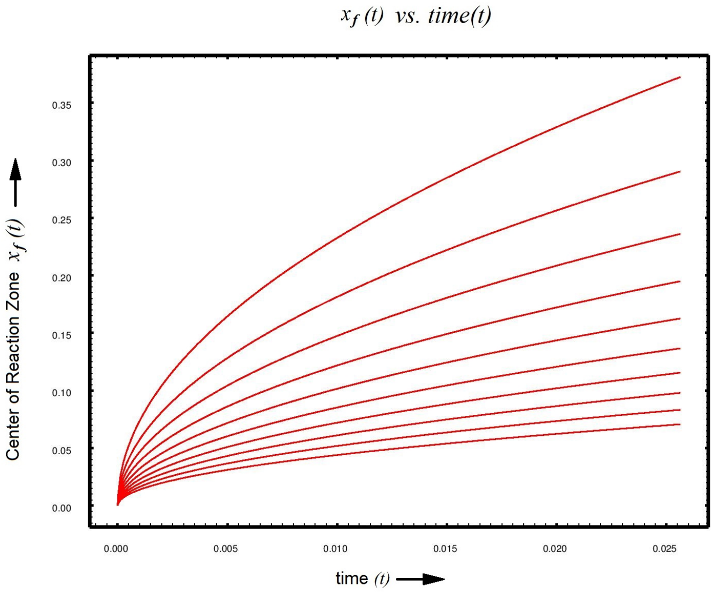

(a) $x_f(t)$ vs. t

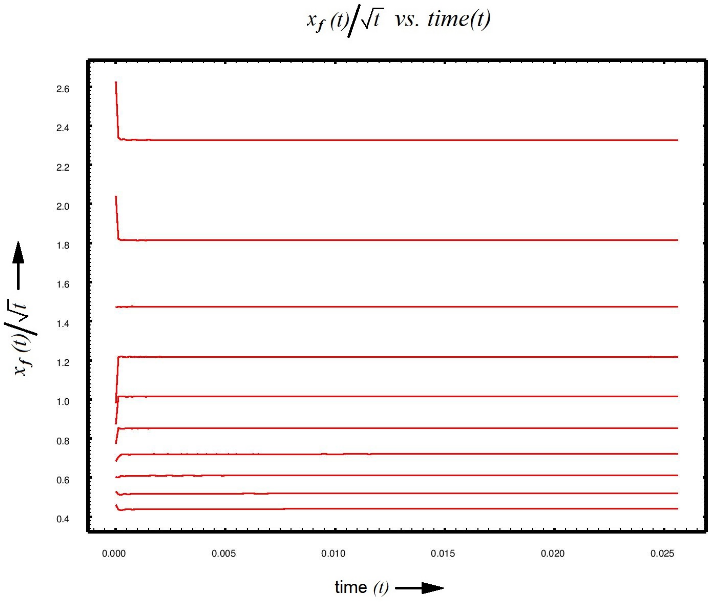

(b) $x_f(t)/\sqrt{t}$ vs. t

Figure 2.23: Center of Reaction Zone for $D_b/D_a = 0.2$ and $(n, m) = (1, 2)$

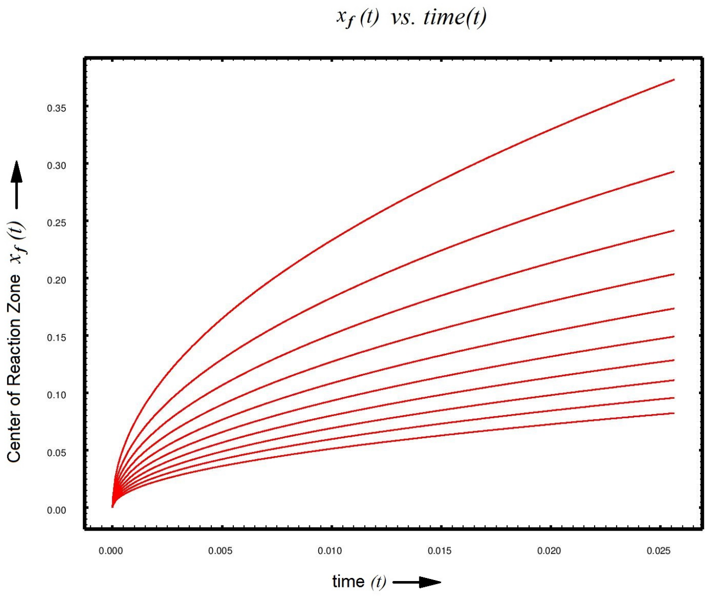

(a) $x_f(t)$ vs. t

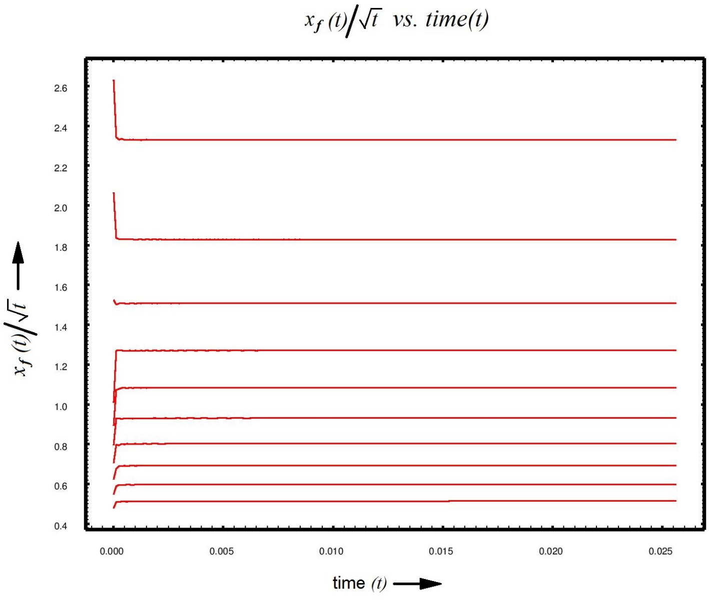

(b) $x_f(t)/\sqrt{t}$ vs. t

Figure 2.24: Center of Reaction Zone for $D_b/D_a = 0.4$ and $(n, m) = (1, 2)$

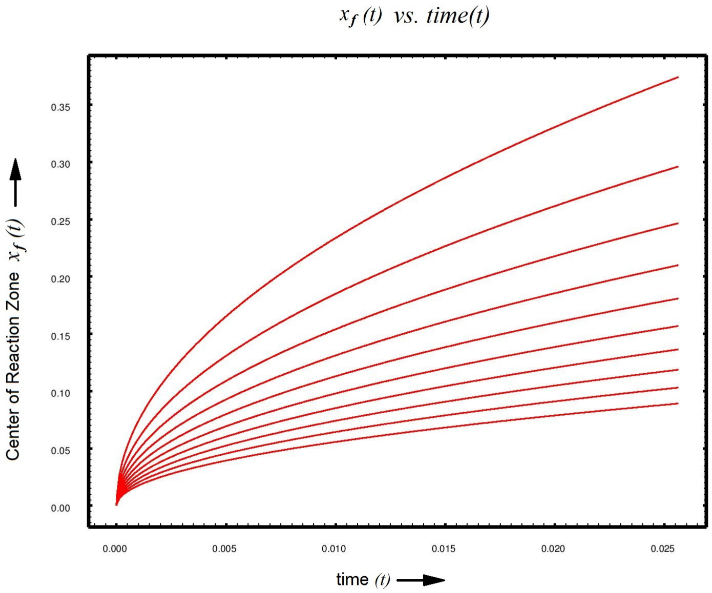

(a) $x_f(t)$ vs. t

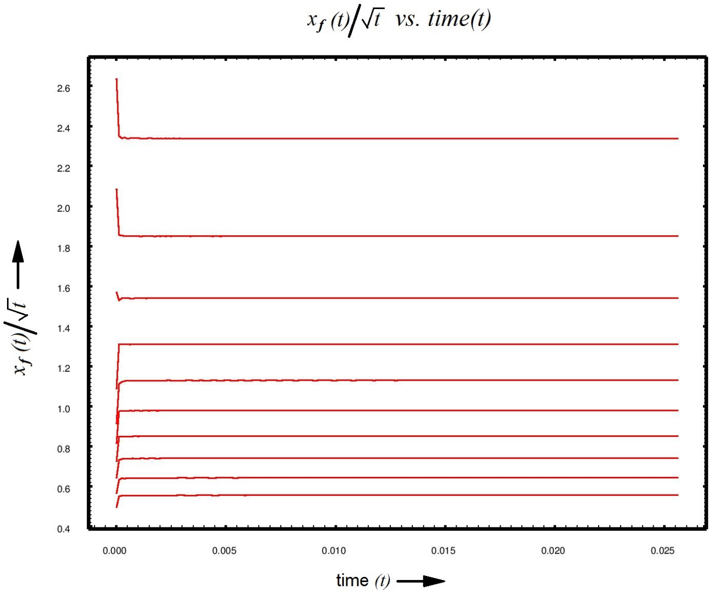

(b) $x_f(t)/\sqrt{t}$ vs. t

Figure 2.25: Center of Reaction Zone for $D_b/D_a = 0.6$ and $(n, m) = (1, 2)$

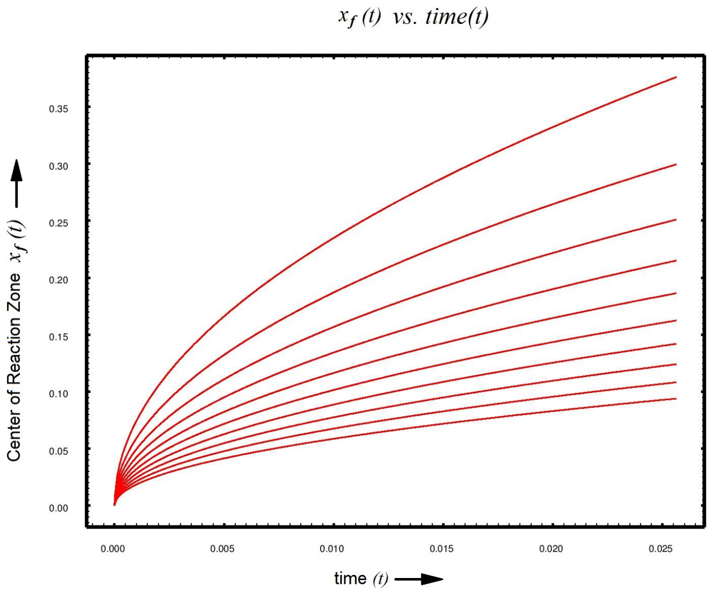

(a) $x_f(t)$ vs. t

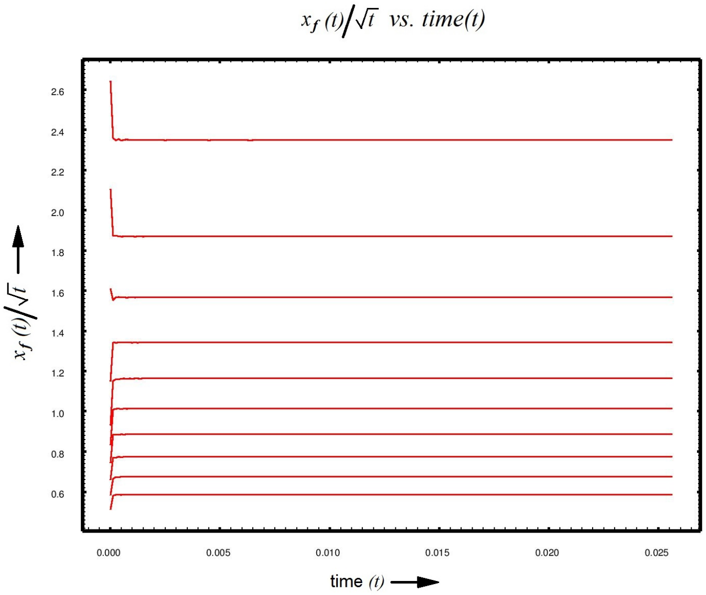

(b) $x_f(t)/\sqrt{t}$ vs. t

Figure 2.26: Center of Reaction Zone for $D_b/D_a = 0.8$ and $(n, m) = (1, 2)$

2.2.3.5 Numerical Results for $D_b/D_a = 1$ and $(n, m) = (2, 1)$

For the sake of presenting enough numerical evidence, we present the results for $(n, m) = (2, 1)$ in this and the next section. Later sections section will present similar results for $(n, m) = (2, 2)$. Qualitatively, the results are similar to those presented in previous two sections. However, it will be observed from numerical results that the center of reaction zone travels in different direction depending on whether $q \leq 0.5$ or $q > 0.5$ respectively. As explained previously, q changes from 0.1 to 1.0 in the steps of 0.1 as one moves from the topmost branch of the graph to the lowest branch.

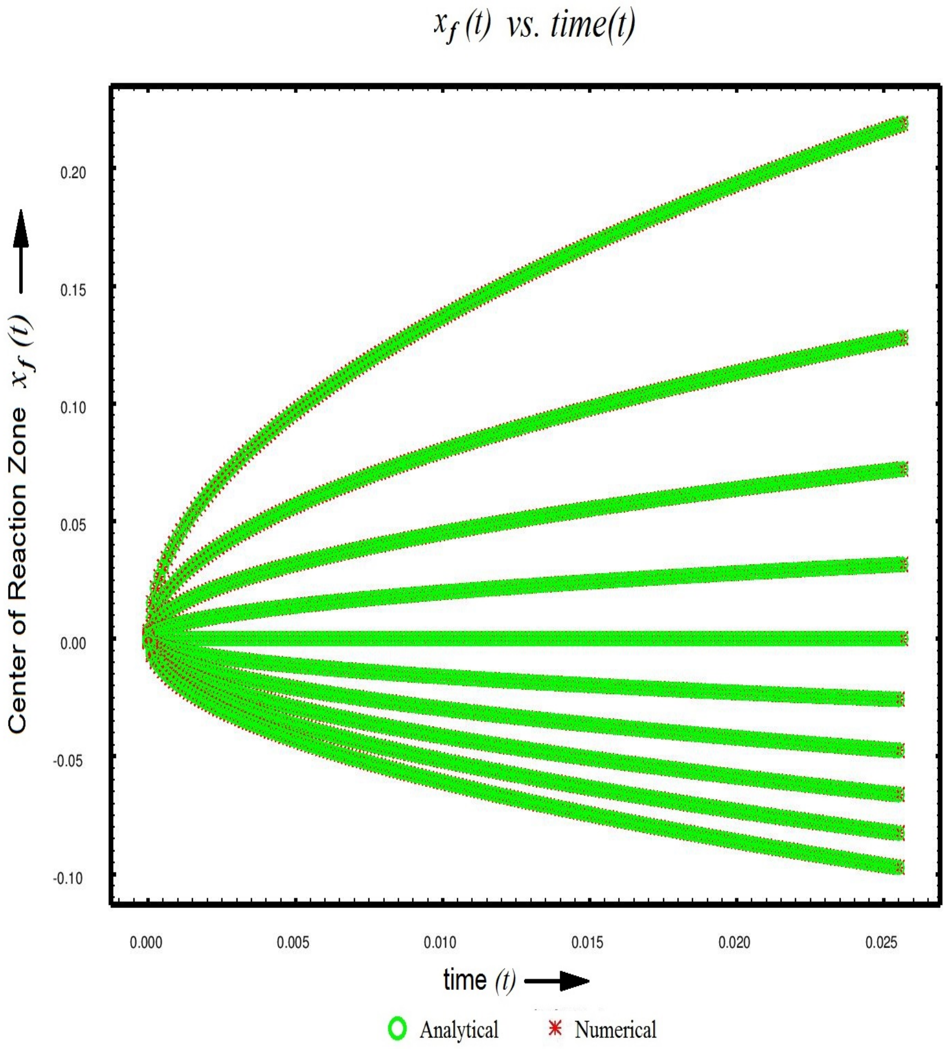

Figure 2.27: Graphical results for $(n, m) = (2, 1)$ Theoretical position of the center of reaction zone is given by $x_f(t) = 2erf^{-1}\left(\frac{1-2q}{1+2q}\right)\sqrt{t}$.

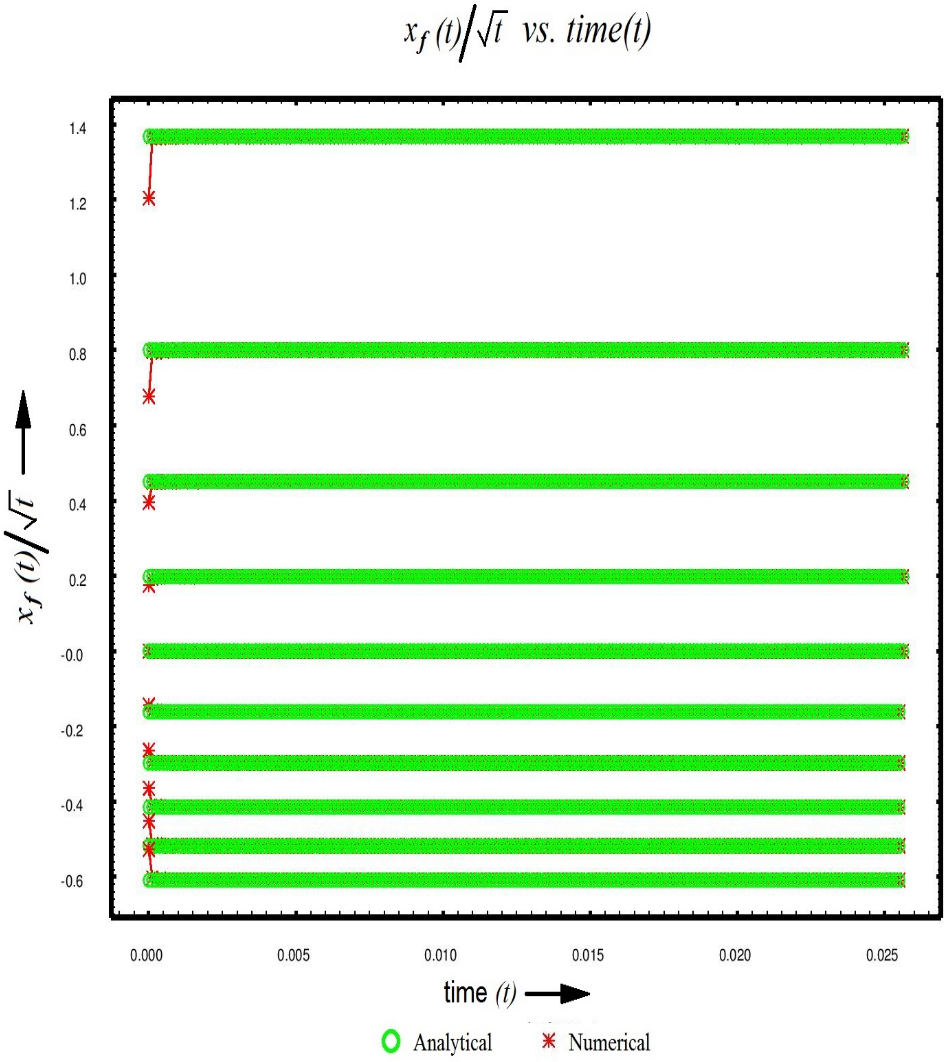

Figure 2.28: Graphical results for $x_f(t)/\sqrt{t}$ vs t for different q's.

2.2.3.6 Numerical Results for $D_b/D_a \neq 1$ and $(n, m) = (2, 1)$

As before, we present the numerical results for $(n, m) = (2, 1)$ and $D_b/D_a = 0.2, 0.4, 0.6$ and 0.8. q changes from 0.1 to 1.0 in the steps of 0.1 as one moves from the topmost branch of the graph to the lowest branch.

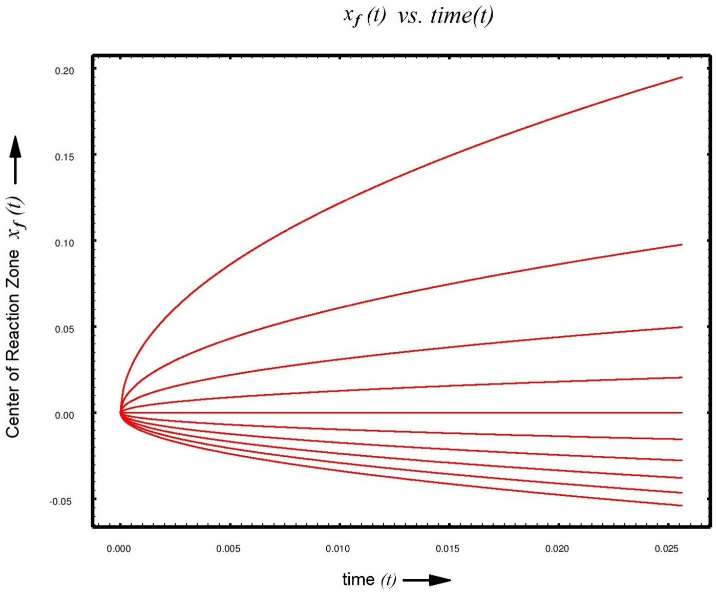

(a) $x_f(t)$ vs. t

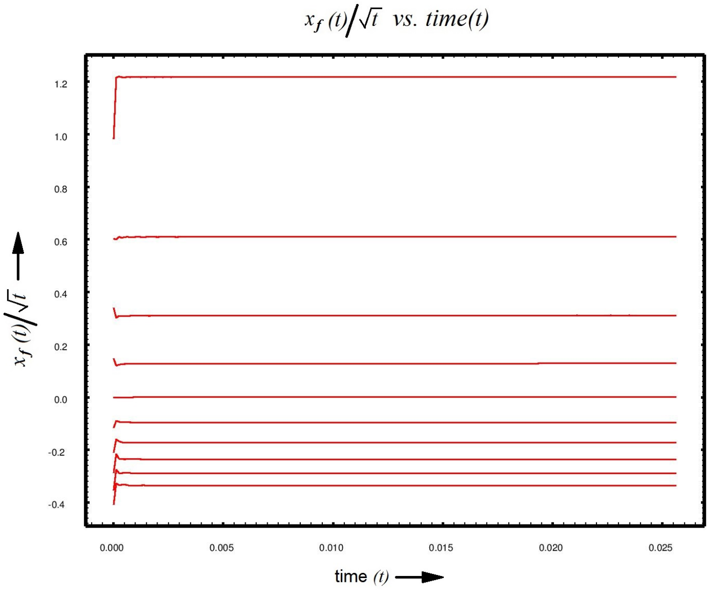

(b) $x_f(t)/\sqrt{t}$ vs. t

Figure 2.29: Center of Reaction Zone for $D_b/D_a = 0.2$ and $(n, m) = (2, 1)$

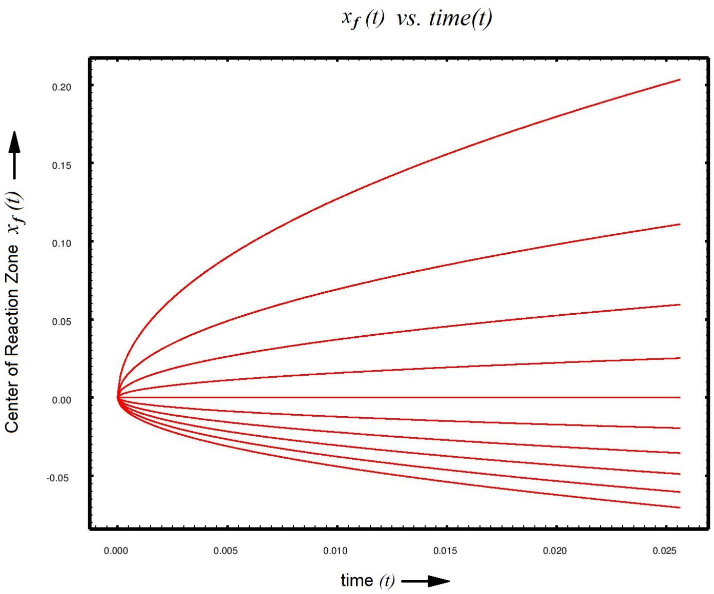

(a) $x_f(t)$ vs. t

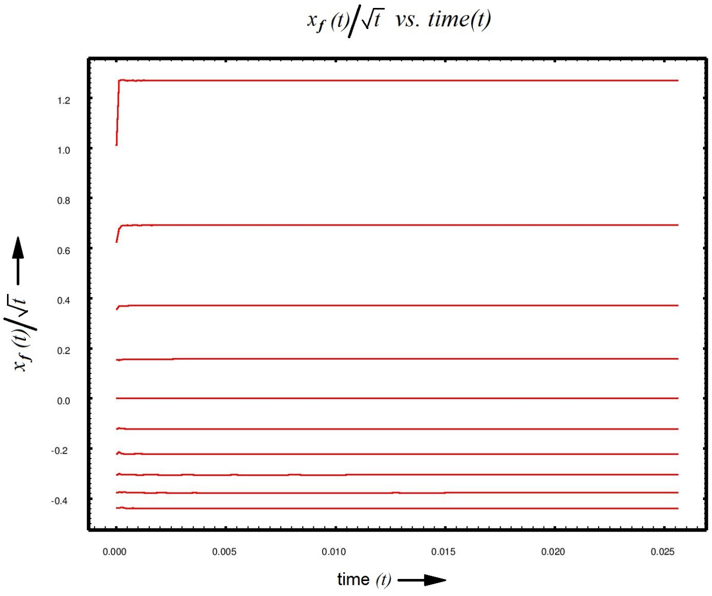

(b) $x_f(t)/\sqrt{t}$ vs. t

Figure 2.30: Center of Reaction Zone for $D_b/D_a = 0.4$ and $(n, m) = (2, 1)$

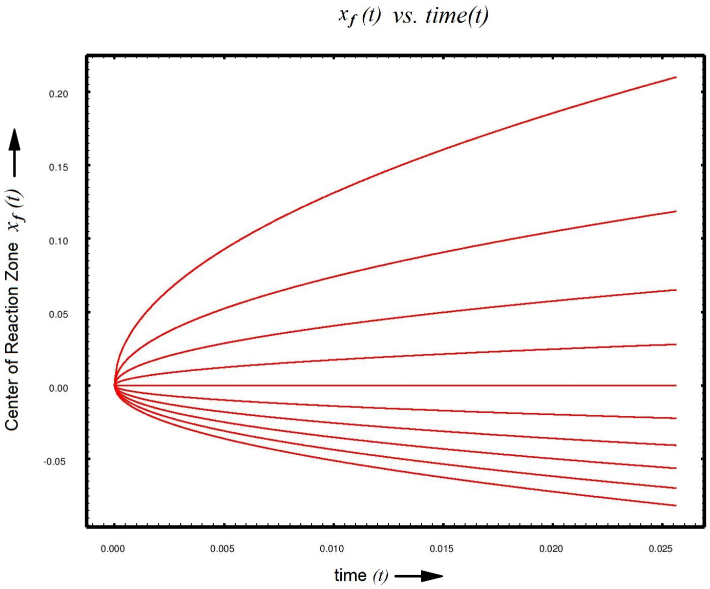

(a) $x_f(t)$ vs. t

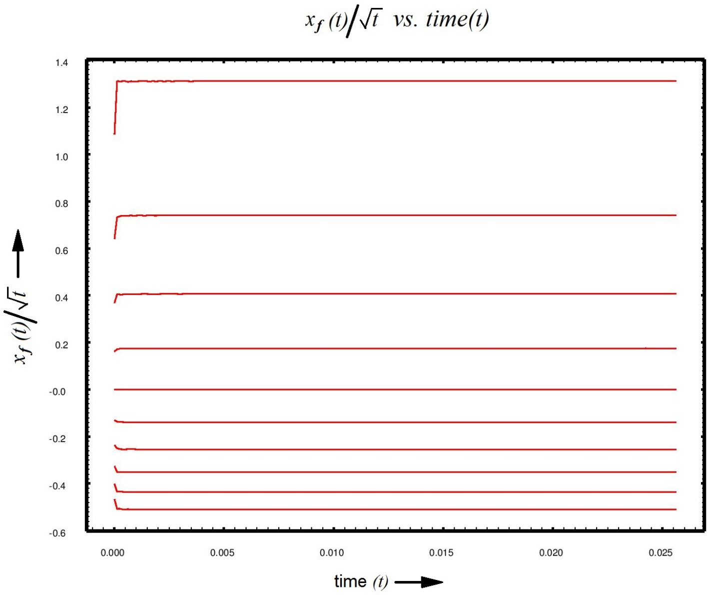

(b) $x_f(t)/\sqrt{t}$ vs. t

Figure 2.31: Center of Reaction Zone for $D_b/D_a = 0.6$ and $(n, m) = (2, 1)$

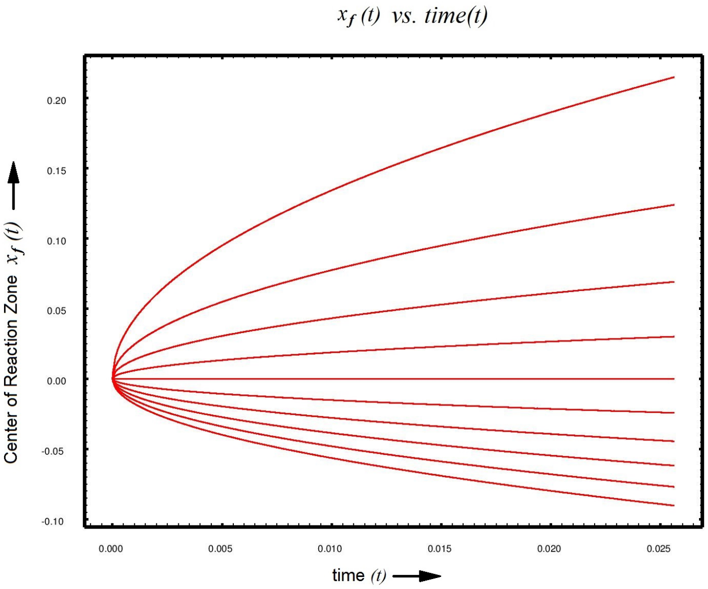

(a) $x_f(t)$ vs. t

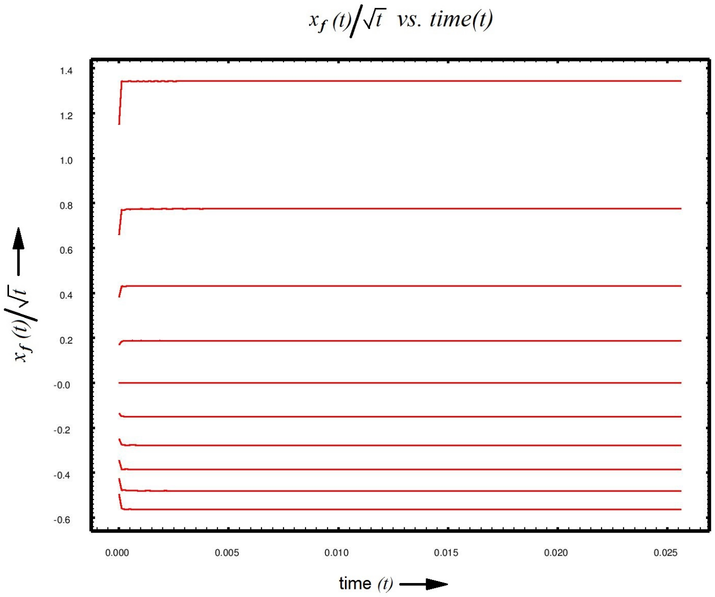

(b) $x_f(t)/\sqrt{t}$ vs. t

Figure 2.32: Center of Reaction Zone for $D_b/D_a = 0.8$ and $(n, m) = (2, 1)$

2.2.3.7 Numerical Results for $D_b/D_a = 1$ and $(n, m) = (2, 2)$

Lastly, we take up the case of $(n, m) = (2, 2)$. We present the theoretical and numerical results for comparison. As before, q changes from 0.1 to 1.0 in the steps of 0.1 as one moves from the topmost branch of the graph to the lowest branch.

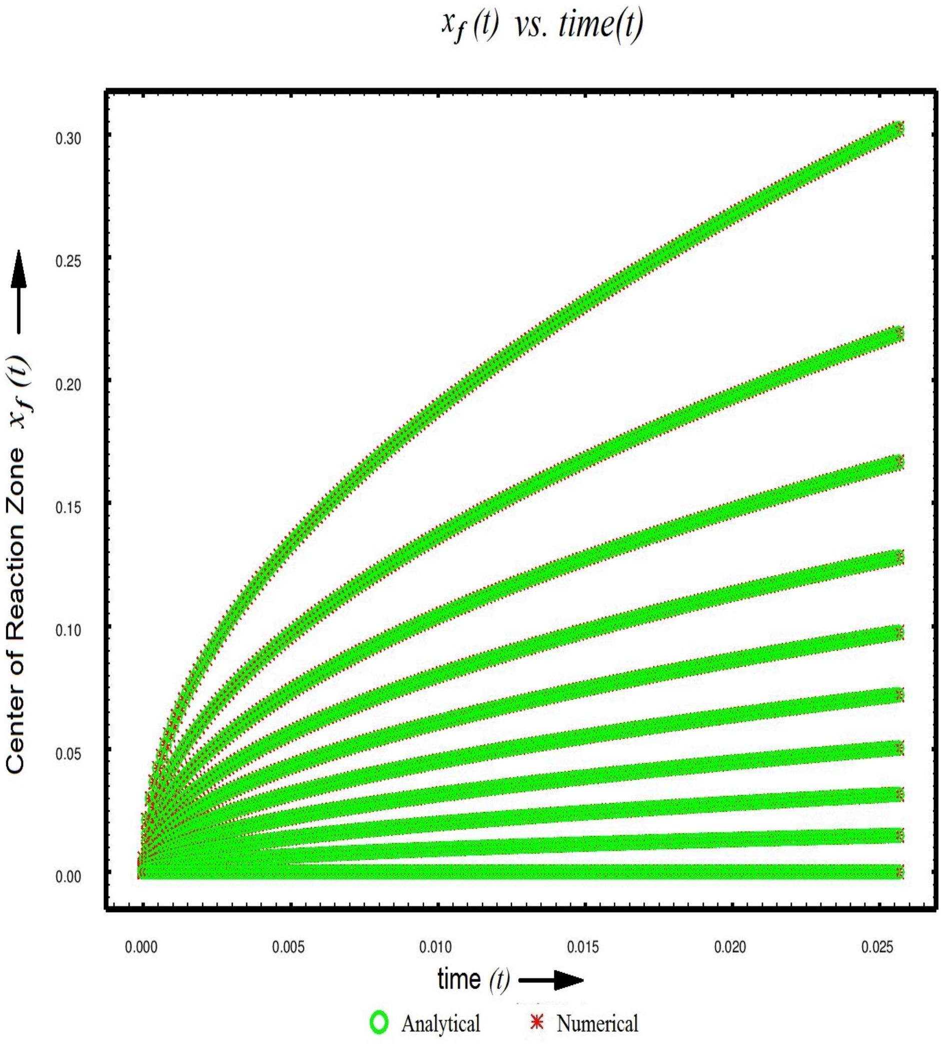

Figure 2.33: Graphical results for $(n, m) = (2, 2)$ Theoretical position of the center of reaction zone is given by $x_f(t) = 2erf^{-1}\left(\frac{1-q}{1+q}\right)\sqrt{t}$.

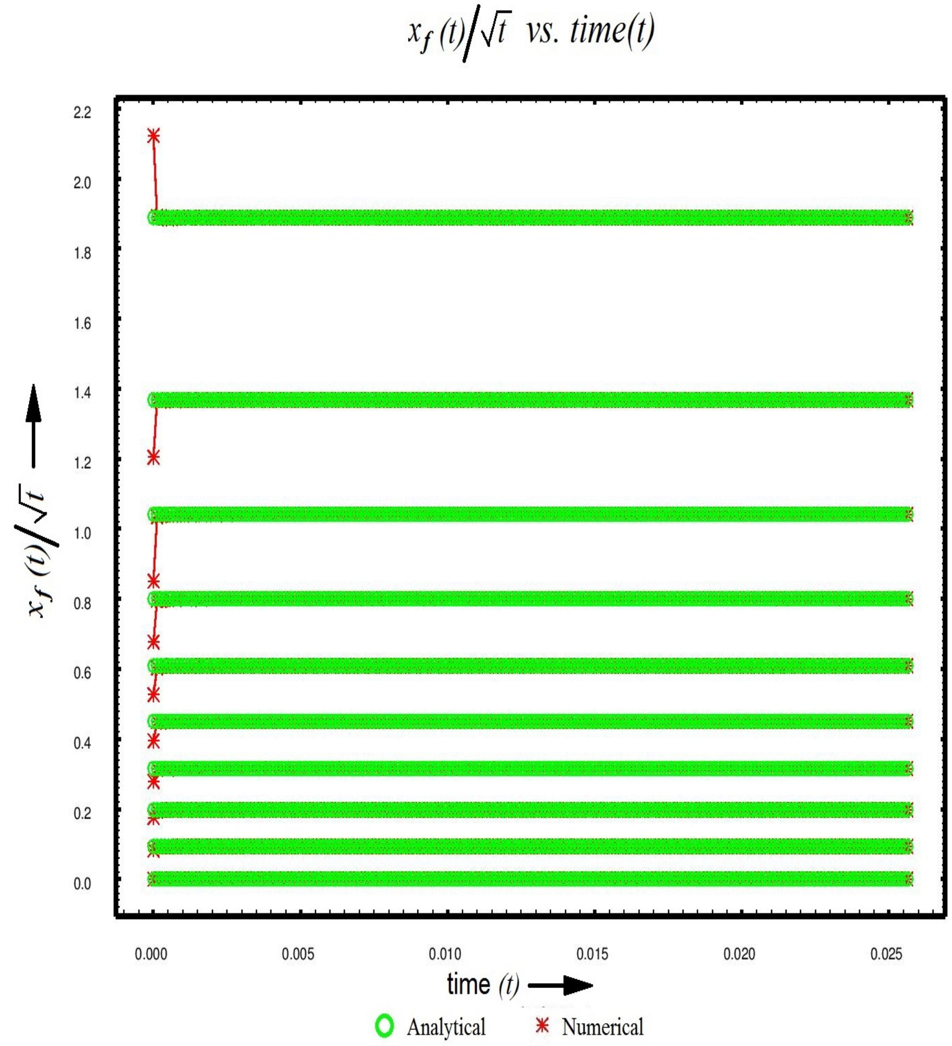

Figure 2.34: Graphical results for $x_f(t)/\sqrt{t}$ vs t for different q's.

2.2.3.8 Numerical Results for $D_b/D_a \neq 1$ and $(n, m) = (2, 2)$

In the graphs which follow (till the end of this subsection), q changes from 0.1 to 1.0 in the steps of 0.1 as one moves from the topmost branch of the graph to the lowest branch.

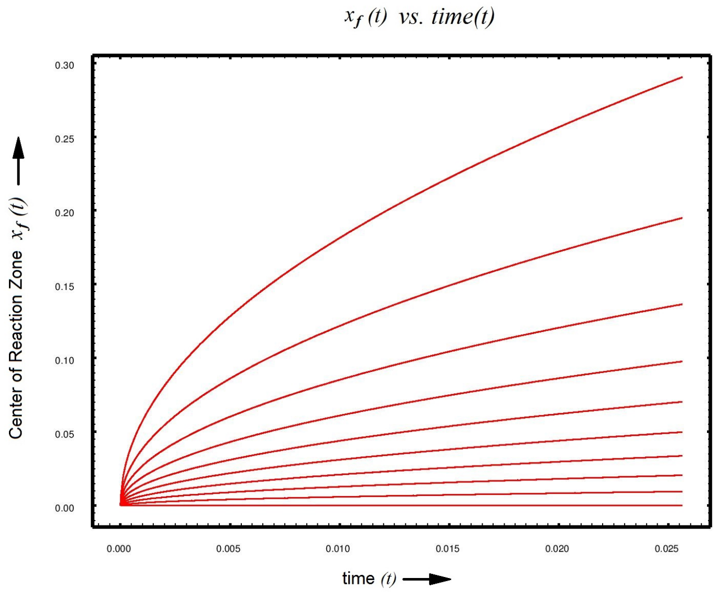

(a) $x_f(t)$ vs. t

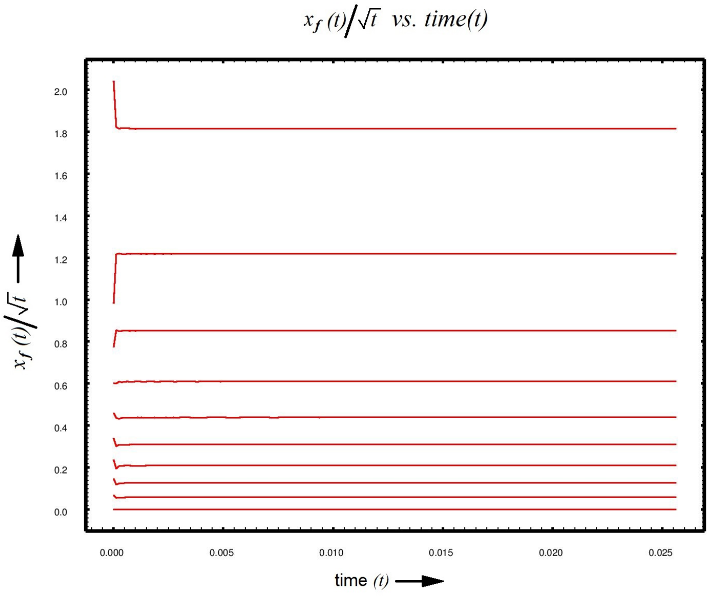

(b) $x_f(t)/\sqrt{t}$ vs. t

Figure 2.35: Center of Reaction Zone for $D_b/D_a = 0.2$ and $(n, m) = (2, 2)$

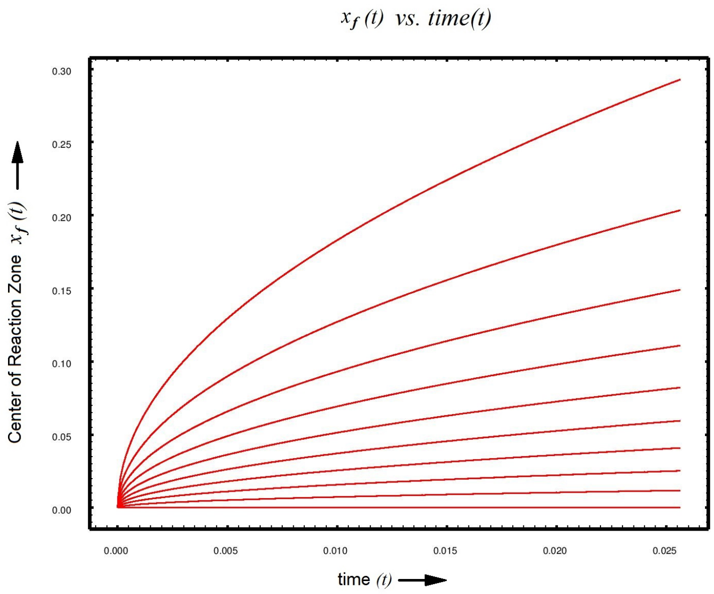

(a) $x_f(t)$ vs. t

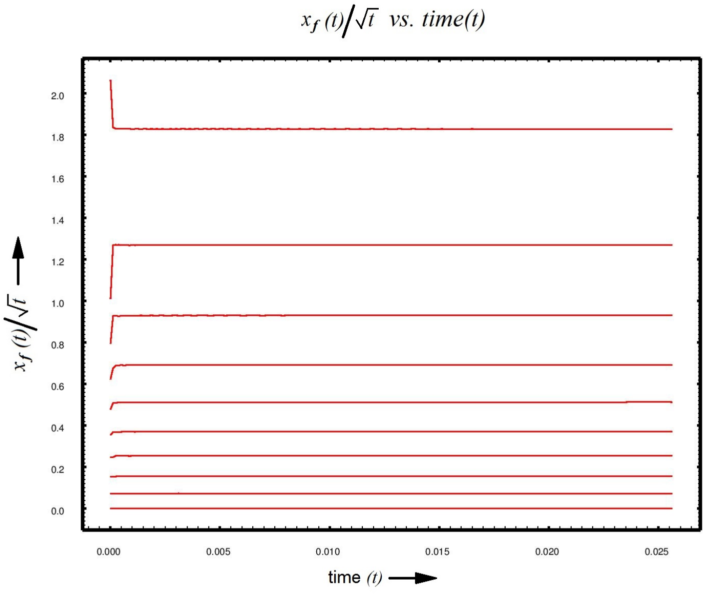

(b) $x_f(t)/\sqrt{t}$ vs. t

Figure 2.36: Center of Reaction Zone for $D_b/D_a = 0.4$ and $(n, m) = (2, 2)$

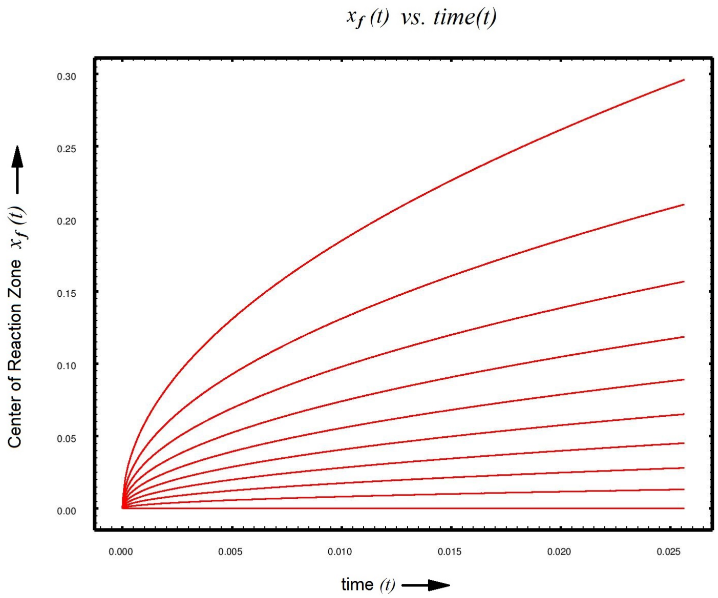

(a) $x_f(t)$ vs. t

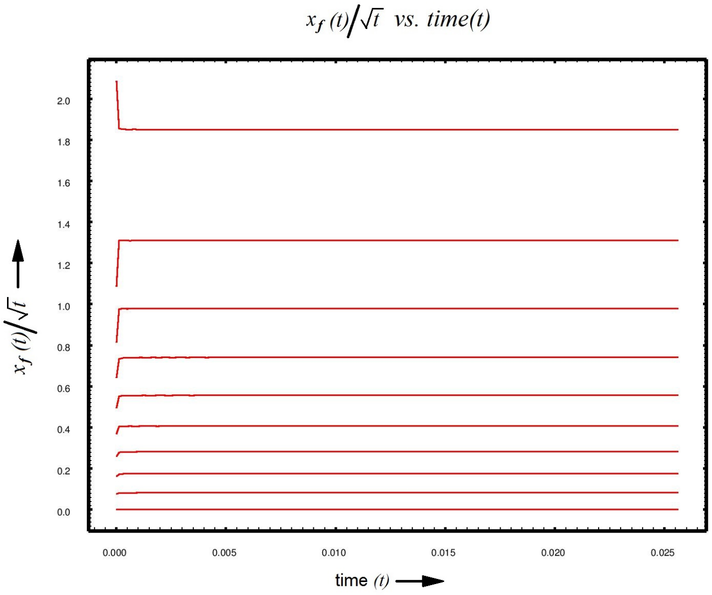

(b) $x_f(t)/\sqrt{t}$ vs. t

Figure 2.37: Center of Reaction Zone for $D_b/D_a = 0.6$ and $(n, m) = (2, 2)$

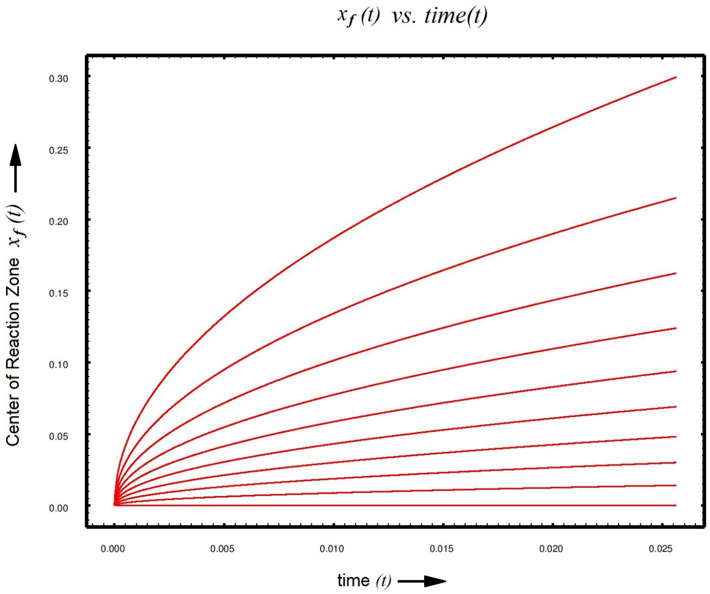

(a) $x_f(t)$ vs. t

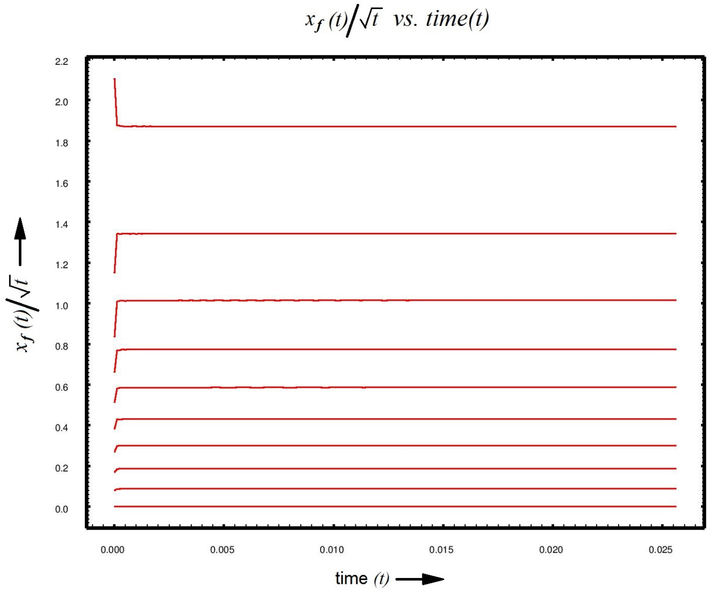

(b) $x_f(t)/\sqrt{t}$ vs. t

Figure 2.38: Center of Reaction Zone for $D_b/D_a = 0.8$ and $(n, m) = (2, 2)$

2.2.3.9 Summary and Conclusion

We have presented enough numerical evidence to support the conjecture that $x_f(t) = \eta\big(D_b/D_a, n, m, q\big)\sqrt{t}$ for every $D_b/D_a, n, m$ and q. Although the results are presented only for $n = 1, 2$ and $m = 1, 2$, and only for a few values of the stated parameters. However, we mention in passing that similar results were obtained for $D_b/D_a = 0.1, 0.2, ...1.0$ and for $q = 0.1, 0.2, ...1.0$, only with minor shape changes. In our opinion, the results are consistent enough to support the claim.

Chapter 3

Front Tracking

The "Front" is defined as the boundary point between two regions containing a sharp discontinuity of a physical variable, e.g. density, concentration, viscocity etc. Theoretically, the function representing the physical variable is not differentiable at a point of discontinuity. This problem can be handled by using the integral form of the governing equations. However, if the numerical scheme is of low order, then the front diffuses quickly losing it's sharpness. On the other hand, a high order numerical scheme may cause numerical oscillations near the front and reduce the high order of accuracy near the region [40]. To solve these difficulties, there exist two main strategies, namely front-capturing and front-tracking.

The main idea of front capturing is to use a high order scheme and use artificial viscosity around the front to diffuse it slightly to avoid oscillations. Front capturing works well for shocks but does not work very well for contact discontinuities[40]. It also requires high resolution.

Second appoach is front tracking in which the front is represented by hypersurface elements (line segments in 2D and triangles in 3D). This approach is best suited sharp discontinuities.

We apply the front tracking method and the FronTier code to study crystal formation in a generic 3 component reaction-diffusion system. We use front tracking to track the position of the front where there is a discontinuity in solute concentration. We then use finite difference scheme (Crank-Nicolson) to update the concentrations of the reactants and the product which are still in the liquid phase.

The front tracking method treats the moving interface as an interior boundary and and applies finite difference method to each subdomain where concentration fields are smooth.

We use the FronTier library to implememnt the front tracking and crystal growth.

The functions implemented in the library can be classified as folloes: [1]

1. **Initialization.** Initialization functions are capable of initializing the problem parameters as well as geometrical parameters for the computations such dimension, domain, computational grid and boundary conditions. This is done through the input routines. Initialization of the interface is also done through these functions as well as the front velocity initialization.

2. **Query Functions.** Query functions are used to obtain information about the front interface such as vertex coordinates, hypersurface elements (bonds in 2D and triangular surface elements in 3D), access to the manifold (hypersurface), tangents and normals to the surface elements etc.

3. **Propagation Control Functions.** These functions include advancement of the front interface, redistribution and bifurcation.

4. **Front and Subdomain Interaction Functions.** These include the functions which couple the PDE solvers with the front interface functions. These functions can be used to obtain information like the nearest grid points, values of the physical variables in a cell/grid point near the interface etc.

5. **Ourput and Data Saving Functions.**These functions mainly deal with the data output which is used for visualization of the simulations. The compatible file types include VTK for VisIt, Paraview, Geomview, HDF and GD packages. These functions also have the capability to halt and/or restart the program run from a specific time or time-step.

Chapter 4

Mathematical Model for Crystal Growth

Consider a reaction-diffusion system given by $nA + mB \longrightarrow C$ and let a seed be already present inside the computational domain. The evolution of concentrations is governed by the following system of equations:

$$\frac{\partial A}{\partial t} = \nabla \cdot (D_A \nabla A) - k_{AB} A^n B^m \tag{4.1}$$

$$\frac{\partial B}{\partial t} = \nabla \cdot (D_B \nabla B) - k_{AB} A^n B^m \tag{4.2}$$

$$\frac{\partial C}{\partial t} = \nabla \cdot (D_C \nabla C) + k_{AB} A^n B^m - k \int_F H(C - C_{eq}) \delta(\vec{x} - \vec{x_f}) d\vec{x_f} \tag{4.3}$$

where $A(\vec{x}, t), B(\vec{x}, t), C(\vec{x}, t)$ are normalized concentrations, D_A, D_B, D_C are diffusion coefficients, $k_{AB} > 0$ is the rate coefficient of homogeneous reaction (liquid phase), $k > 0$ is the rate coefficient of heterogeneous reaction (precipitation), $\vec{x_f}$ is a point on fluid-solid interface and C_{eq} is the equilibrium concentration. $H(\cdot)$ represents the Heaviside step function and $\delta(\cdot)$ represents the dirac-delta function. The integration is taken over the whole fluid-solid interface.

The fluid-solid interface is advanced with the normal velocity:

$$\nu_n(\vec{x_s}) = -\frac{1}{\rho_s} D_C \frac{dC}{dn} \tag{4.4}$$

where ρ_s is the crystal density and dC/dn is the normal derivative of the concentration $C(\vec{x}, t)$.

The FronTier code has the ability to detect if a cell contains liquid phase or solid phase. We use this capability and for purely liquid phase, we note that the integral $k \int_F H(C - C_{eq})\delta(\vec{x} - \vec{x_f})d\vec{x_f} = 0$. Assuming that a computational cell contains only liquid phase and that the diffusion coefficients stay constant throughout the liquid phase, the system of equations is reduced to:

$$\frac{\partial A}{\partial t} = D_A \nabla^2 A - k_{AB} A^n B^m \tag{4.5}$$

$$\frac{\partial B}{\partial t} = D_B \nabla^2 B - k_{AB} A^n B^m \tag{4.6}$$

$$\frac{\partial C}{\partial t} = D_C \nabla^2 C + k_{AB} A^n B^m \tag{4.7}$$

Any high order finite difference scheme may be used to solve this system of equations. In the present work, we have used Crank-Nicolson scheme.

When a cell contains purely solid phase, we assume that there is neither reaction nor diffusion taking place. Thus there is no need to solve the system for the cells containing purely solid phase.

When a cell contains fluid-solid interface, both liquid and solid phases are present inside the cell. At a point of interface, $k \int_F H(C - C_{eq})\delta(\vec{x} - \vec{x_f})d\vec{x_f} = kH(C - C_{eq})$. To update the concentrations at the grid point of a cell containing the interface, we introduce ghost points in the opposite direction to that of the interface and then solve the system using finite differences. The ghost points are introduced to maintain second order accuracy of the finite difference scheme.

Once the concentrations are updated, we propagate the fluid-solid interface by the methods described by Li et al.[1]. To update the concentrations at a point on the interface, we assume that the solute concentrations at the fluid-solid interface are $A_s = B_s = 0$. Thus, for the $(n+1)$-th time step, the discretized equation for C_s is given by:

$$\frac{C_s^{(n+1)} - C_s^{(n)}}{\Delta t} = \left(D_C \frac{C_{s+h}^{(n+1)} - C_s^{(n+1)}}{h} - kH(C_s^{(n+1)} - C_{eq}) \right) \frac{2}{h} \tag{4.8}$$

where h is the spatial step in normal direction. The superscripts denote time step.

Chapter 5

Numerical Results

In this section, we present the numerical results which show the effects of different parameters of the problem on the crystal growth. The parameters which control the reaction-diffusion system described by equations (4.1) to (4.3) are D_A, D_B, D_C and k_{AB}, k.

We set the computational domain to a square $[0, 1] \times [0, 1]$. The boundary conditions used for testing are $A(x, 0, t) = B(x, 1, t) = 0$ and $A(x, 1, t) = B(x, 0, t) = 1$.

5.1 Effects of k_{AB} and k

We first explore the effects of k_{AB} and k on the crystal growth. We present the simulation results for different shapes of initial seeds, namely rectangular, circular and triangular. Initial conditions used were $A(x, y, 0) = g_1(y)$ and $B(x, y, 0) = f_1(y)$, where f_1 and g_1 are the functions described in section 2.1.2. We have also used only first order reaction. i.e. $(n, m) = (1, 1)$.

It can be observed from the following tests that the dendritic growth is pronounced when k is high. k_{AB} has negligible effect on the dendritic growth. It will also be observed that in general, the direction in which dendrites grow is controlled by D_A/D_B. This point will be further explored in the next section.

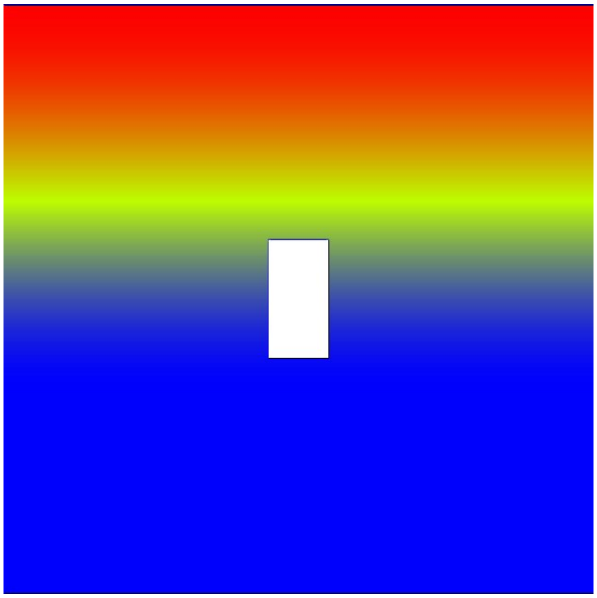

(a) $t = 0$

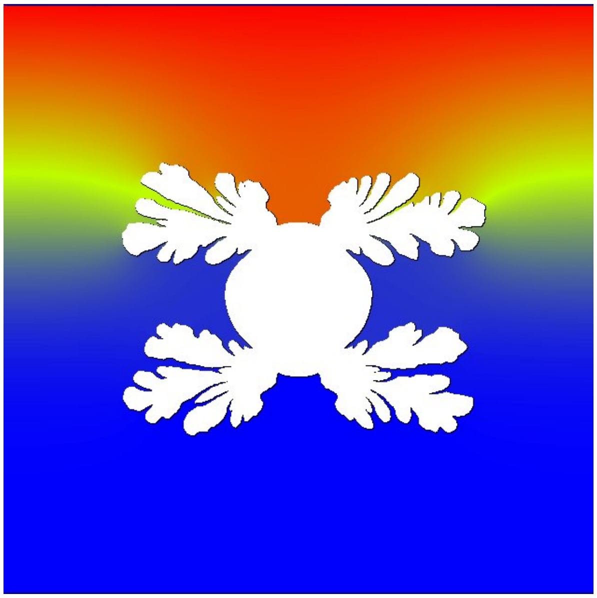

(b) $t = 2.755$

Figure 5.1: Parameters are $k_{AB} = 150$, $k = 800$ and $D_A = D_B = D_C = 0.5$

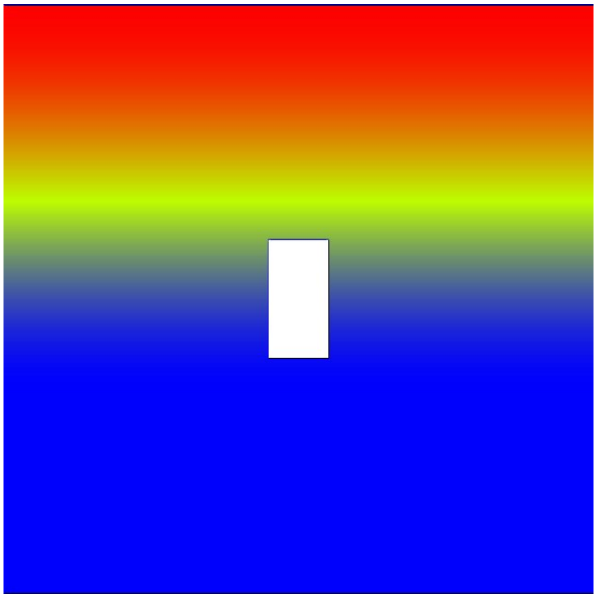

(a) $t = 0$

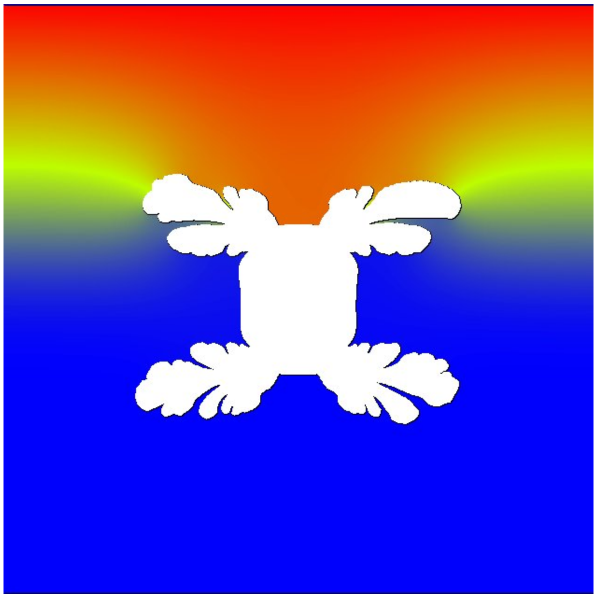

(b) $t = 2.755$

Figure 5.2: Parameters are $k_{AB} = 1500$, $k = 200$ and $D_A = D_B = D_C = 0.5$

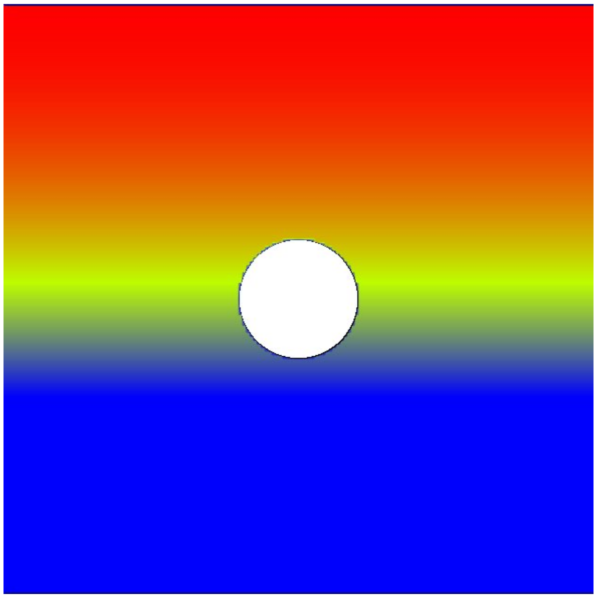

(a) $t = 0$

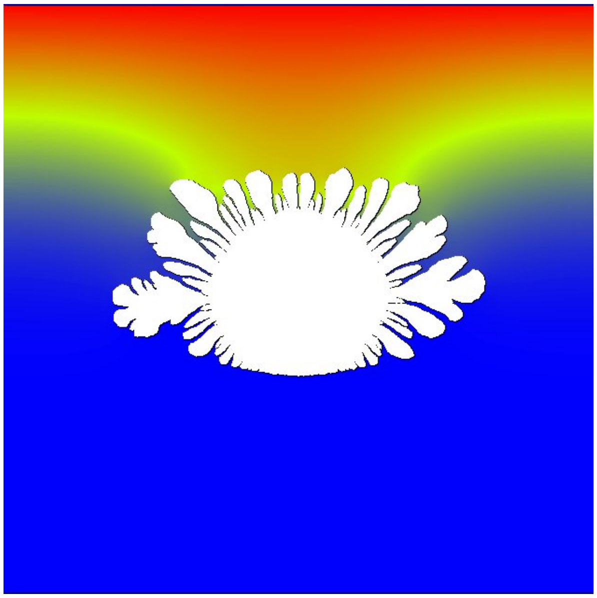

(b) $t = 2.755$

Figure 5.3: Parameters are $k_{AB} = 150$, $k = 800$ and $D_A = 0.3$, $D_B = 0.7$, $D_C = 0.5$

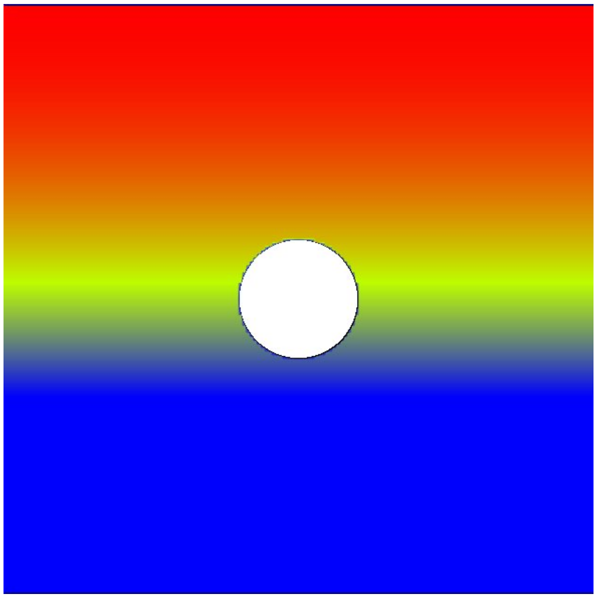

(a) $t = 0$

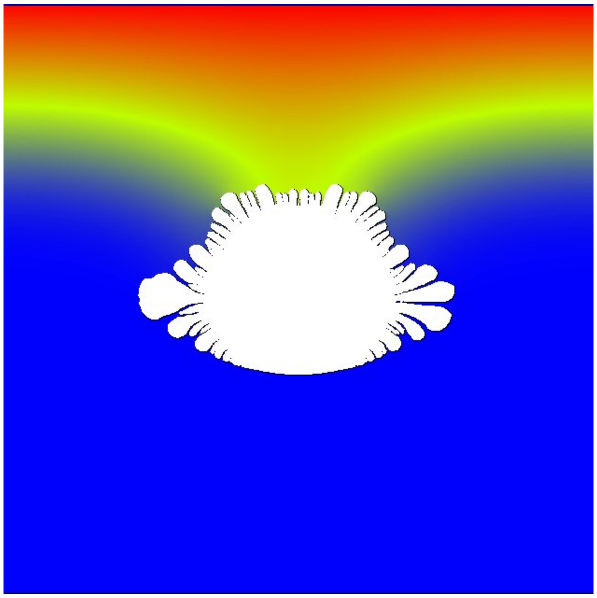

(b) $t = 2.755$

Figure 5.4: Parameters are $k_{AB} = 1500$, $k = 200$ and $D_A = 0.3$, $D_B = 0.7$, $D_C = 0.5$

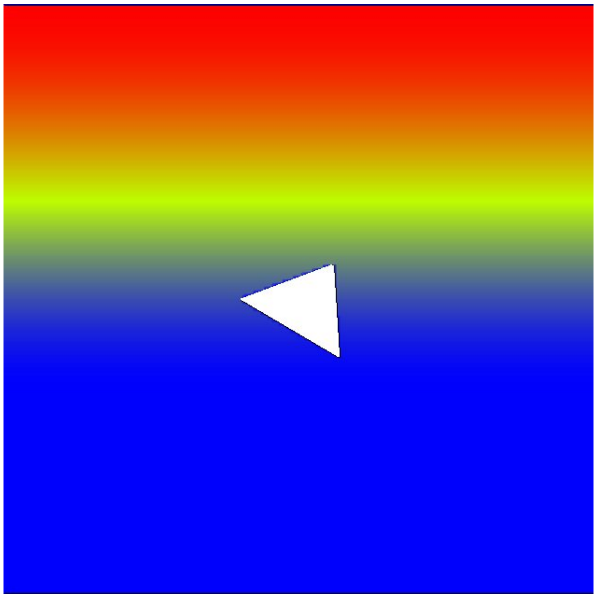

(a) $t = 0$

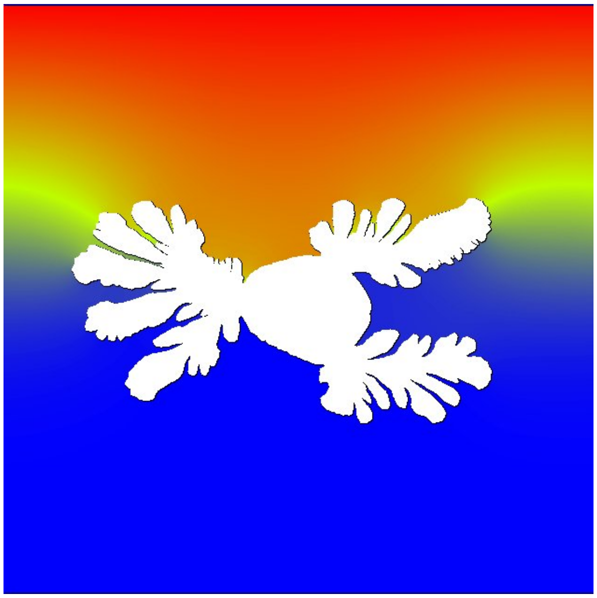

(b) $t = 2.755$

Figure 5.5: Parameters are $k_{AB} = 150$, $k = 800$ and $D_A = 0.3$, $D_B = 0.7$, $D_C = 0.5$

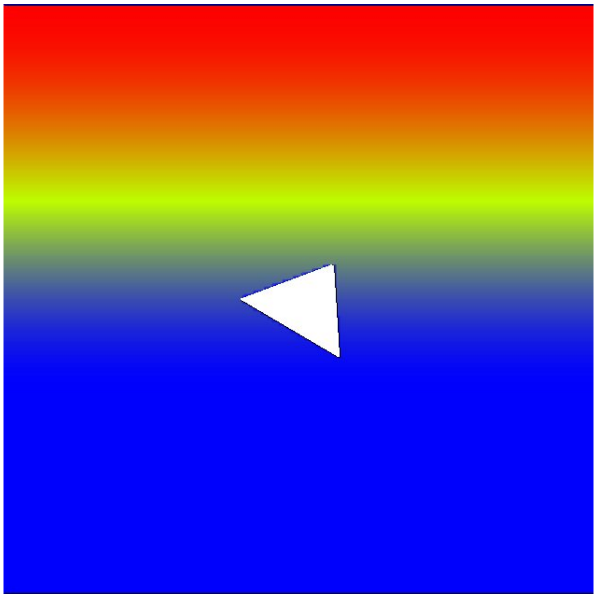

(a) $t = 0$

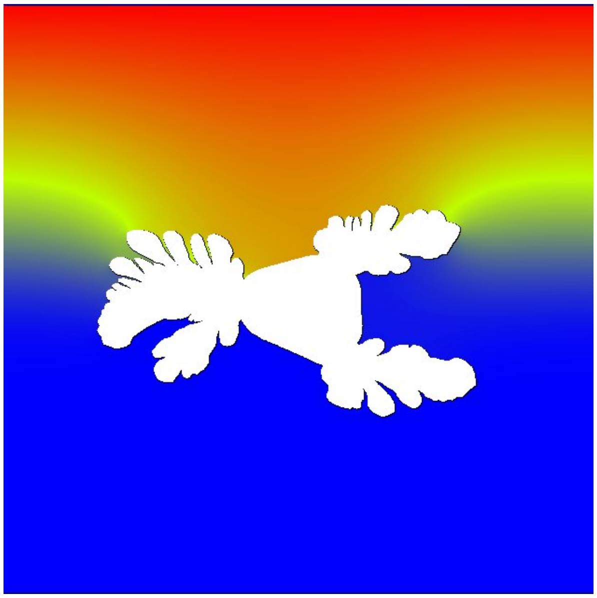

(b) $t = 2.755$

Figure 5.6: Parameters are $k_{AB} = 1500$, $k = 200$ and $D_A = 0.3$, $D_B = 0.7$, $D_C = 0.5$

5.2 Effect of the diffusivities

As mentioned in the previous section, the direction in which the dendrites grow is controlled by the value of D_A/D_B. This is explored more in this section. The initial conditions vary for each simulation. However, initial conditions are found to have little effect on the direction of growth.

(a) $D_A = 0.3$, $D_B = 0.7$

(b) $D_A = 0.5$, $D_B = 0.5$

(c) $D_A = 0.7$, $D_B = 0.3$

Figure 5.7: Parameters are $k_{AB} = 150$, $k = 800$ and $D_C = 0.5$. Each image is taken at $t = 2.68$.

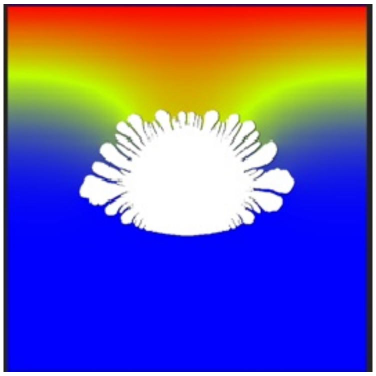

(a) $D_A = 0.3$, $D_B = 0.7$

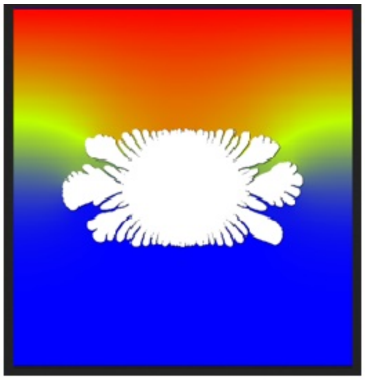

(b) $D_A = 0.5$, $D_B = 0.5$

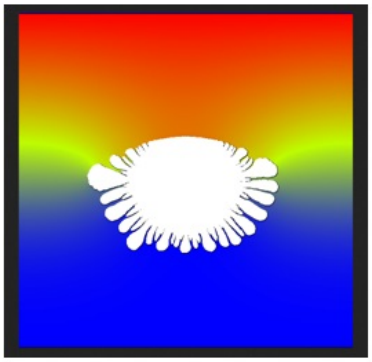

(c) $D_A = 0.7$, $D_B = 0.3$

Figure 5.8: Parameters are $k_{AB} = 150$, $k = 800$ and $D_C = 0.5$. Each image is taken at $t = 2.68$.

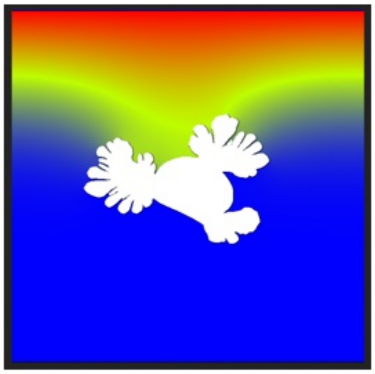

(a) $D_A = 0.3$, $D_B = 0.7$

(b) $D_A = 0.5$, $D_B = 0.5$

(c) $D_A = 0.7$, $D_B = 0.3$

Figure 5.9: Parameters are $k_{AB} = 150$, $k = 800$ and $D_C = 0.5$. Each image is taken at $t = 2.68$.

5.3 Effect of the Damkohler Number

The Damkohler Number, d, is defined by $d = kL/D_C$ [1, 2] where k is the heterogeneous reaction constant, L is the characteristic length and D_C is the diffusion coeficient for the product C. Damkohler number is closely tied with the dendritic growth of the crystal. High Damkohler number produces high dendritic structure and vice-versa. In this section, we provide numerical results which show that the dendritic growth in a RDS for $A + B \longrightarrow C$ occurs only when the Damkohler number is higher than a threshold value. In most of our simulations, the threshold was in the range of 60 to 80. Although it is difficult to predict the exact value of the threshold, we mention that traces of the dendritic structures started to appear for $d = 60$ and they were well formed for $d = 80$. For lower Damkohler numbers, the crystal growth was smooth without any dendrites. The direction of the growth was still controlled by D_A/D_B. The initial shape of the seed had no effect on the threshold value.

The computational domain is $[0, 1] \times [0, 1]$. Reactants A and B are initially separated at $y = 0.5$. Other parameters are as follows: $k_{AB} = 1500$, $D_A = 0.3$, $D_B = 0.7$. We wish to mention that the simulations were carried out for a range of Damkohler Numbers, in particular for $d = 0.1, 0.5, 1, 5, 10, 20, 40, 60, 80, 160$. For small values of d, the crystal growth was not qualitatively different, the only significant difference being the amount of growth in a given time. We also carried out the simulations for a range of values of D_A and D_B. Numerical results showed difference in the direction of crystal growth.

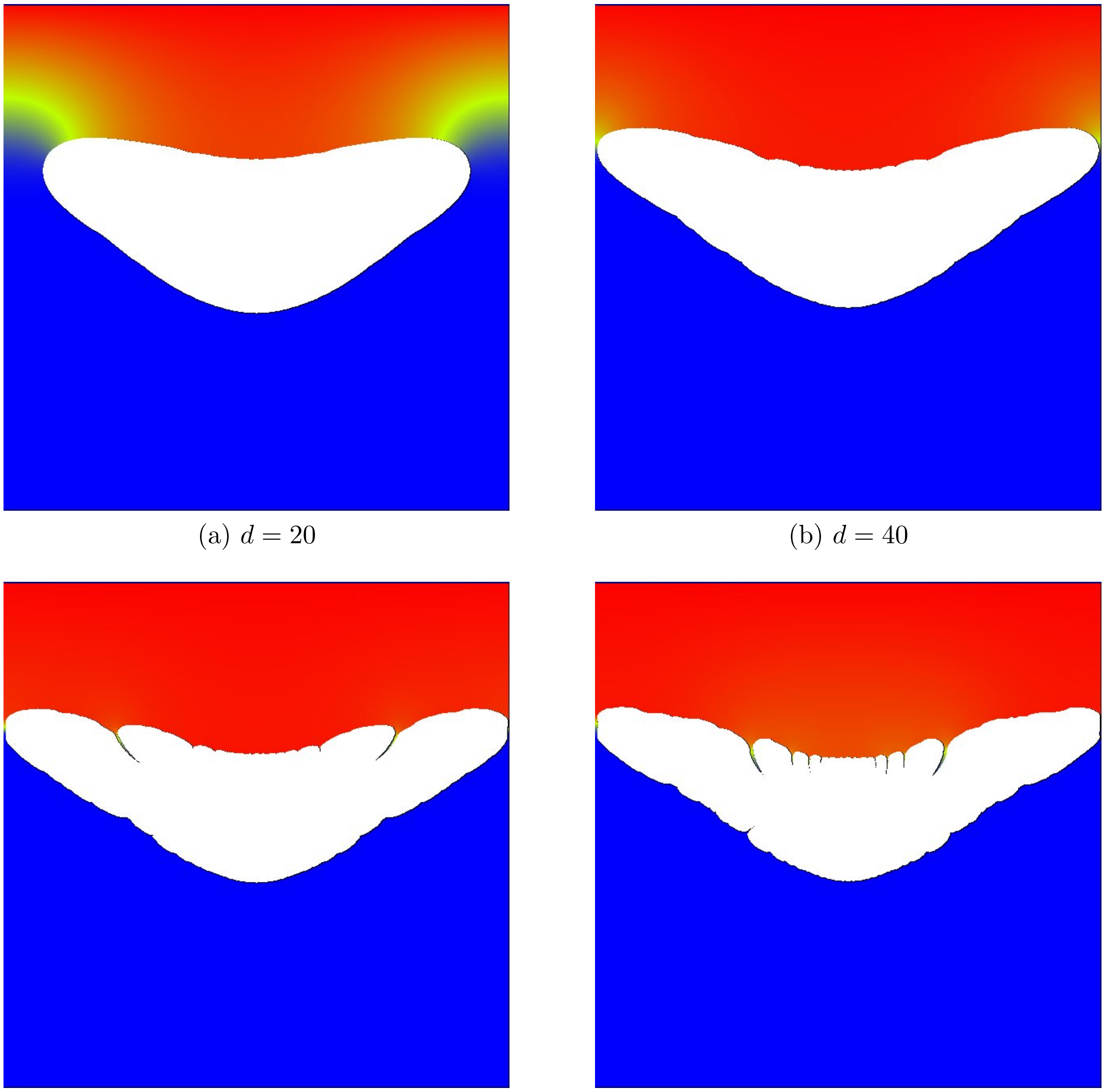

(a) $d = 20$ (b) $d = 40$ (c) $d = 60$ (d) $d = 80$

Figure 5.10: Effects of the Damkohler Number. Parameters are $k_{AB} = 1500$, $D_A = 0.3$ and $D_B = 0.7$. Each image is taken at $t = 2.57$. Initial seed is circular.

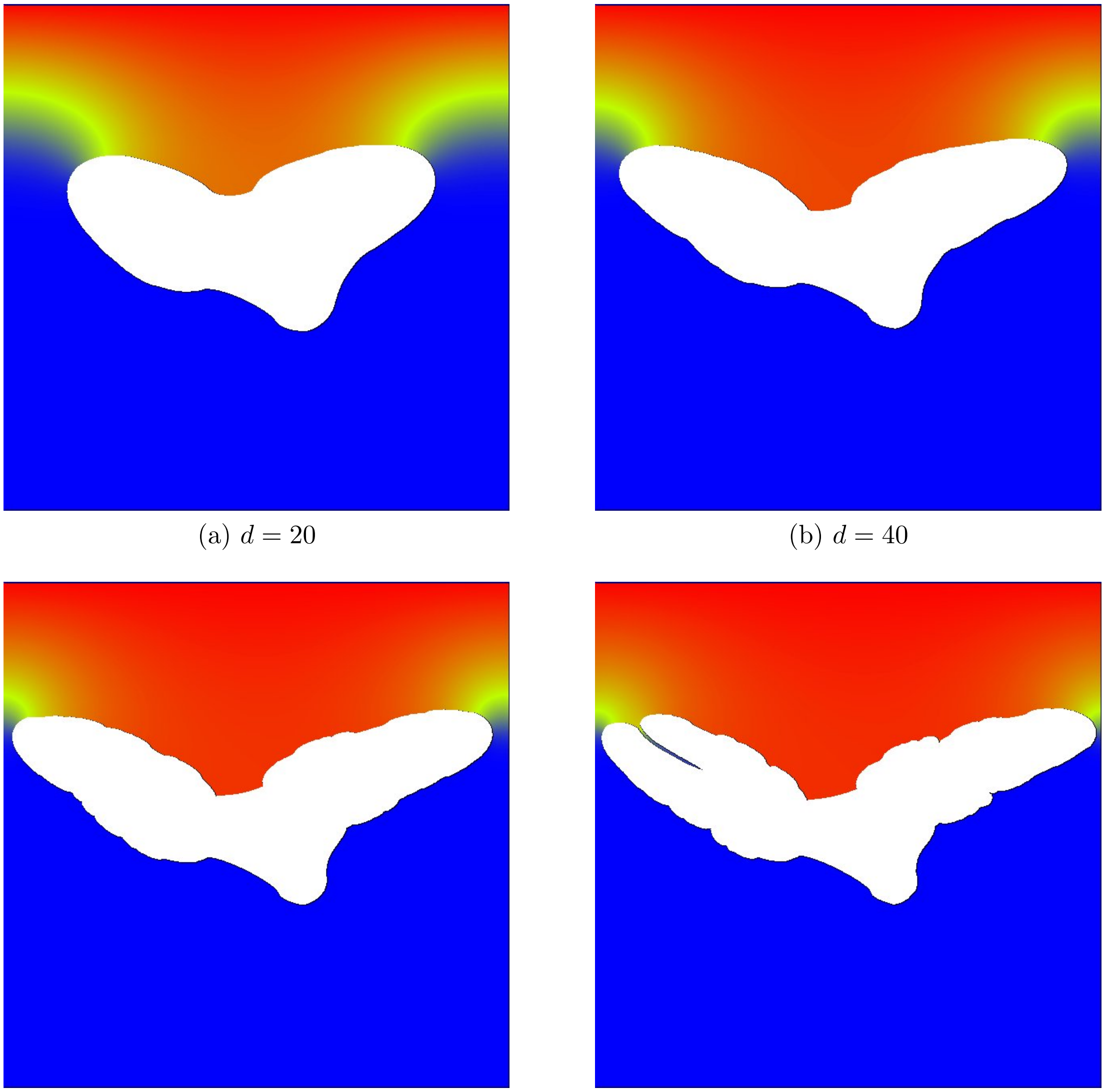

(a) $d = 20$

(b) $d = 40$

(c) $d = 60$

(d) $d = 80$

Figure 5.11: Effects of the Damkohler Number. Parameters are $k_{AB} = 1500$, $D_A = 0.3$ and $D_B = 0.7$. Each image is taken at $t = 2.57$. Initial seed is triangular.

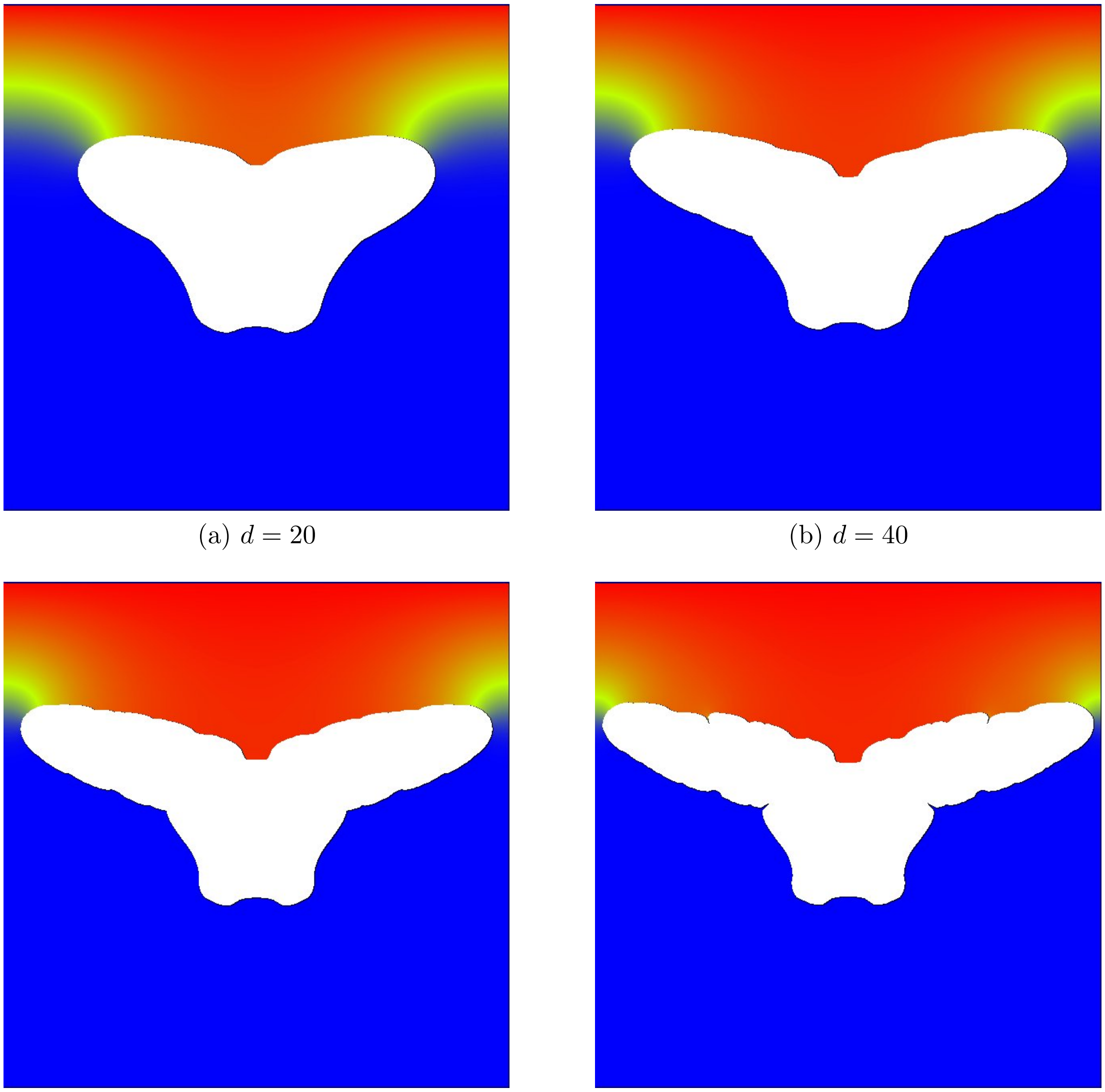

(a) $d = 20$

(b) $d = 40$

(c) $d = 60$

(d) $d = 80$

Figure 5.12: Effects of the Damkohler Number. Parameters are $k_{AB} = 1500$, $D_A = 0.3$ and $D_B = 0.7$. Each image is taken at $t = 2.57$. Initial seed is rectangular.

5.4 Effect of the equilibrium concentration

The supersaturation theory asserts that the deposition of mass occurs only when $C_s > C_{eq}$ where C_s is the concentration of C at a point on the fluid-solid interface and C_{eq} is the equilibrium concentration. The theory also asserts that once the concentration C attains the equilibrium concentration, the deposition occurs instantaneously. It is natural expect that this process will have effect on the dendritic growth. This is confirmed by the following numerical results. Lower equilibrium concentration produces more dendritic growth and vice-versa, when all other parameters are held constant. Parameters used are $k_{AB} = 1500$, $k = 100$, $D_A = 0.3$, $D_B = 0.7$ and $D_C = 0.5$. Other computational setup is the same as the previous sections.

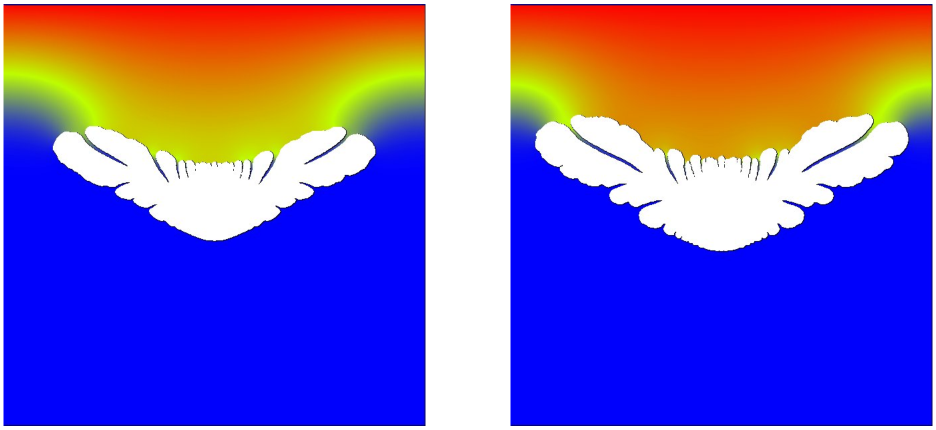

(a) $C_{eq} = 0.1$ (b) $C_{eq} = 0.01$

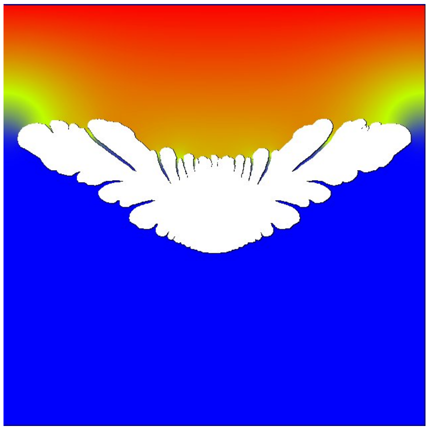

(c) $C_{eq} = 0.001$

Figure 5.13: Effects of the Equilibrium Concentration. Parameters are $k_{AB} = 1500$, $k = 100$, $D_A = 0.3$, $D_B = 0.7$ and $D_C = 0.5$. Each image is taken at $t = 2.629$. Initial seed is circular.

Chapter 6

Conclusions and future directions for research

In the present work, we presented a numerical study of the reaction-diffusion system for the generic reaction $nA + mB \longrightarrow C$. In the study of effectively one dimensional systems, we put forward a conjecture based on the results obtained by other researchers regarding the case of equal diffusivities. Next we provided the nmerical evidence for the case of unequal diffusivities for $(n, m) = (1, 1), (1, 2), (2, 1), (2, 2)$.

In our work on the higher dimensional simulations involving the crystal growth, we examined the effects of parameters D_A, D_B, D_C and k_{AB}, k. We found that the dendritic growth is controlled dominantly by the heterogeneous reaction constant k and the homogeneous reaction constant k_{AB} has no effect on the dendrites. We also observed that the direction in which the dendrites grow is controlled by D_A/D_B. Numerical simulations show that the Damkohler number produces dendritic growth only if it's value is higher than some threshold. The threshold for the particular tests done appears to be in the range of $d = 60$ to $d = 80$. The equilibrium concentration, C_{eq} also has effect on the dedrites with lower C_{eq} being responsible for higher dendritic growth and vice-versa.

The work done here presents a basis for further study of Liesegang Pattern formation in effectively one dimensional systems and multidimensional systems. In particular, the theories put forth for formation of Liesegang Patterns do not adequately explain the spacing and width laws, especially in 2 and 3 dimensions. Out of the theories proposed, the supersaturation theory is especially amenable to the Front Tracking method. It is our contention that front tracking method be used to investigate if supersaturation theory can adequately explain the spacing and width laws in higher dimensions, for which there does not yet exist a fully satisfactory theoretical explanation. Present work and the front tracking code employed can further be used in this direction.

Bibliography

[1] Study of crystal growth and solute precipitation through front tracking method, *Acta Mathematica Scientia, Volume 30, Issue 2, March 2010, Pages 377-390,* Xiaolin Li, James Glimm, Xiangmin Jiao, Charles Peyser, Yanhong Zhao

[2] Numerical simulations of phase transition problems with explicit interface tracking, *Chemical Engineering Science 128(2015) 92-108,* Yijing Hu, Qiangqiang Shi, Valmor F. De Almeida, Xiaolin Li

[3] Hybrid Simulations of Reaction-Diffusion Systems in Porous Media, *SIAM J. Sci. Comput. 30 2799 (2008),* A. M. Tartakovsky, D. M. Tartakovsky, T. D. Scheibe, and P. Meakin

[4] Reaction-Diffusion Cellular Automata Model for the Formation of Liesegang Patterns, *Phys. Rev. Lett. 72, 1384-1387 (1994),* B. Chopard, P. Luthi and M. Droz

[5] Wilhelm Ostwald, *Lehrbuch der Allgemeinen Chemie II/2,* W. Engelmann, Leipzig (1896-1902)

[6] Patterns Produced by Precipitation at a Moving Reaction Front, *Phys. Rev. Lett. 57, 275-278 (1986),* G. T. Dee

[7] Measurements and Hypothesis on Periocic Precipitation Processes, *J. Phys. Chem. 91, 6300-6308 (1987),* M. E. LeVan and J. Ross

[8] Derivation of the Matalon-Packter law for Liesegang paterns, *J. Chem. Phys. 109, 9479-9486 (1998),* T. Antal, M. Droz, J. Magnin, Z. Racz and M. Zrnyi

[9] The Liesegang Phenomenon. I. Sol Protection and Diffusion, *J. Colloid Sci. 10, 46-61 (1955),* R. Matalon and A. Packter

[10] Pattern Formation in a New Class of Precipitation Reactions, *Ph.D. Thesis, Peter Hantz,* UNIVERSITÉ DE GENÈVE

[11] Chemistry and Crystal Growth, *Angew. Chem. Int. Ed. Engl. 33, 143-162 (1994),* Jurg Hulliger

[12] Dendrites, Viscous Fingers, and the Theory of Pattern Formation, *Science 243, 1150-1156 (1989),* J. S. Langer

[13] Competition between kinetic and surface tension anisotropy in dendritic growth, *Eur. Phys. J. B 16, 337-344 (2000),* T. Ihle

[14] Diffusion-Limited Aggregation: A Model for Pattern Formation, *Physics Today 53, 36-41 (2000),* Thomas C. Halsey

[15] Mathematical Analysis of the Formation of Periodic Precipitates, *J. Colloid Sci. 5, 85-97 (1950),* C. Wagner

[16] Periodic Precipitation Patterns in the Presence of Concentration Gradients 1., *J. Phys. Chem. 86, 4078-4087 (1982),* Stefan C. Muller, Shoichi Kai and John Ross

[17] The Formation of Liesegang Rings as a Periodic Coagulation Phenomenon, *Journal of the Chemical Society 1928/II, 2714-2727 (1928),* Ernest S. Hedges and Rosalind V. Henley

[18] Mechanism of chemical instability for periodic precipitation phenomena, *J. Chem. Phys. 60, 3458-3465 (1974),* Michael Flicker and John Ross

[19] The Concentration Distribution in the Gel before the Periodic Precipitation, *Memoirs of the Faculty of Science, Kyushu University, Series C Chemistry, 5, 33-42 (1962),* Hiroshige Higuchi and Ryohei Matura

[20] Nucleation and Spinodal Decomposition, *Solid State Phenomena 56, 67-106 (1997),* L. Granasy

[21] Phase Transitions and Critical Phenomena, *vol. 8, Academic Press, London (1989),* C. Domb and J. L. Lebowitz (editors)

[22] Formation of Liesegang Patterns, *Physica A 274, 50-59 (1999),* Zoltan Racz

[23] Pattern formation induced by ion-selective surfaces: Models and simulations, *J. Chem. Phys. 123, 034707 (2005),* Szabolcs Horvt and Pter Hantz

[24] Properties of the reaction front in an $A + B \longrightarrow C$ type reaction-diffusion process, *Physical Review A 1988, Volume 38, Number 6: 3151-3154,* L. Galfi and Z. Racz

[25] Properties of the asymptotic $nA + mB \longrightarrow C$ reaction-diffusion fronts, *Eur. Phys J. B 17 (2000): 673-678,* J. Magnin

[26] Dynamic multiscaling of the recation-diffusion front for $mA + nB \longrightarrow C$, *Physical Review E, October 1995, Volume 52, Number 4,* S. Cornell, Z. Koza and M. Droz

[27] Reaction front for $A + B \longrightarrow C$ diffusion-reaction systems with initially separated reactants, *Physical Review A, July 1992, Volume 46, Number 2,* H. Larralde, M. Araujo, S. Havlin and H. Stanley

[28] Steady-State Reaction-Diffusion Front Scaling for $mA + nB \longrightarrow C$, *Physical Review Letters, June 1993, Volume 70, Number 24,* S. Cornell and M. Droz

[29] Asymptotic behaviour of initially separated $A+B_{(static)} \longrightarrow C$ reaction-diffusion systems, *Physica A 240 (1997) 622-634,* Z. Koza

[30] Reaction-Diffusion fronts in systems with concentration-dependent diffusivities, *Physical Review E 74, 036103 (2006),* P. Polanowski and Z. Koza

[31] Reaction fronts in reversible $A + B \rightleftharpoons C$ reaction-diffusion systems, *Physica A 330 (2003) 160-166,* Z. Koza

[32] Reversible and irreversible reaction fronts in two competing reaction system, *Nuclear Instruments and Methods in Physica Research B 186 (2002) 161-165,* M. Sinder, H. Taitelbaum, J. Pelleg

[33] Asymptotic expansion for reversible $A + B \longleftrightarrow C$ reaction-diffusion process, *Physical Review E 66, 011103 (2002),* Z. Koza

[34] The Long-time Behavior of Initially Separated $A + B \longrightarrow C$ Reaction-Diffusion Systems with Arbitrary Diffusion Constants, *J. Stat. Phys. 85, 179-191(1996),* Z. Koza

[35] Some Properties of the $A + B \longrightarrow C$ Reaction-Diffusion System with Initially Separated Components, *Journal of Statistical Physics, Vol. 65, Nos. 5/6, 1991,* H. Taitelbaum, S. Havlin, J. Kiefer, B. Trus, and G. Weiss

[36] Numerical analysis of reversible $A + B \longleftrightarrow C$ reaction-diffusion systems, *Eur. Phys. J. B 32, 507-511(2003),* Z. Koza

[37] Simulation study of reaction fronts, *Physical Review A, December 1990, Volume 42, Number 12,* Z. Jiang and C. Ebner

[38] Refined simulations of the reaction front for diffusion-limited two-species annihilation in one dimension, *Physical Review E, May 1995, Volume 51, Number 5,* S. Cornell

[39] Role of fluctuations for inhomogeneous reaction-diffusion phenomena, *Physical Review A, Volume 44, Number 8, Oct. 1991,* S. Cornell, M. Droz, B. Chopard

[40] A Front-Tracking Method for Viscous, Incompressible, Multi-fluid Flows *Journal of Computational Physics 100, 25-37 (1992)* Salih Ozen Unverdi, Gretar Tryggvason

[41] Numerical simulation of dendritic solidification with convection: Two-Dimensional Geometry, *Journal of Computational Physics, Volume 180, Issue 2, 10 August 2002, Pages 471-496*, Nabeel Al-Rawahi, Gretar Tryggvason

[42] Numerical simulation of dendritic solidification with convection: Three-dimensional flow, *Journal of Computational Physics, Volume 194, Issue 2, 1 March 2004, Pages 677-696*, Nabeel Al-Rawahi, Gretar Tryggvason

[43] Front tracking for gas dynamics, *Journal of Computational Physics, Volume 62, Issue 1, January 1986, Pages 83-110*, I.-L Chern, J. Glimm, O. Mcbryan, B. Plohr, S. Yaniv

[44] A simple package for front tracking, *Journal of Computational Physics, 213:613-628, 2006*, Jian Du, Brian Fix, James Glimm, Xicheng Jia, Xiaolin Li, Yunhua Li, and Lingling Wu

[45] A level set simulation of dendritic solidification with combined features of front-tracking and fixed-domain methods, *Journal of Computational Physics, 211:36-63, 2006*, Lijian Tan and Nicholas Zabaras

[46] Front tracking in two and three dimensions, *Comput. Math. Appl., 35(7):1-11, 1998*, J. Glimm, M. J. Graham, J. W. Grove, X.-L. Li, T. M. Smith, D. Tan, F. Tangerman, and Q. Zhang

[47] Frontier and applications to scientific and engineering problems, *Proceedings of International Congress of Industrial and Applied Mathematics, pages 1024507 - 1024508, 2008*, W. Bo, B. Fix, J. Glimm, X. L. Li, X. T. Liu, R. Samulyak, and L. L. Wu

[48] Diamond crystsal growth by plasma chemical vapor deposition, *Journal of Applied Physics, 63:1744-1748, 1988*, C.P. Chang, D.L. Flamm, D.E.Ibbostson, and J.A.Mucha

[49] Precipitation and dissolution of reactive solutes in fractures, *Water Resources Research, 34:457-470, 1998*, Peter Dijk and Brian Berkowitz

[50] Simulation of dissolution and precipitation in porous media, *J. Geophys. Res., 108:2505, 2003*, Q. Kang, D. Zhang, and S. Chen

[51] Numerical modeling of ice deposition, *Journal of the Atmospheric Sciences, 28:226-237, 1970*, L. R. Koenig

[52] An experimental investigation of nonaqueous phase liquid dissolution in saturated subsurface systems: Steady state mass transfer rates, *Water Resources Research, 28:2691-2705, 1992*, Susan E. Powers, Linda M. Abriola, and Walter J. Weber JR